

Analysis of Tandem Bubble Interaction and Jet Formation in a Microfluidic Channel

by

Chen Yang

Department of Mechanical Engineering and Materials Science
Duke University

Date: _____

Approved:

Pei Zhong, Supervisor

Edward J Shaughnessy

Laurens E Howle

Thesis submitted in partial fulfillment of
the requirements for the degree of
Master of Science in the Department of
Mechanical Engineering and Materials Science in the Graduate School
of Duke University

2013

ABSTRACT

Analysis of Tandem Bubble Interaction and Jet Formation in a Microfluidic Channel

by

Chen Yang

Department of Mechanical Engineering and Materials Science
Duke University

Date: _____

Approved:

Pei Zhong, Supervisor

Edward J Shaughnessy

Laurens E Howle

An abstract of a thesis submitted in partial
fulfillment of the requirements for the degree
of Master of Science in the Department of
Mechanical Engineering and Materials Science in the Graduate School of
Duke University

2013

Copyright by
Chen Yang
2013

Abstract

Tandem bubble interactions have been shown to produce jets that can be used to create membrane poration on single cells, and jet speed has been implicated as a critical parameter for tandem bubble-induced bioeffects. In this thesis, the dynamics of single and tandem bubbles in a microfluidic channel ($25 \times 800 \mu\text{m}$ in height and width) are investigated to assess the effects of bubble size on tandem bubble interaction and resultant jet. Experimentally, the dynamics of bubble oscillation produced by laser irradiation of a gold dot (15 nm thick and $6 \mu\text{m}$ in diameter) coated on the glass substrate of the microfluidic channel are captured by a high-speed camera, from which the time history of bubble size and jet speed are determined. Numerically, the bubble dynamics are simulated using 3DynaFS-BEM (DYNAFLOW, INC.) based on a potential flow model solved by boundary element method (BEM). By adjusting the initial conditions in the BEM code, the dynamics of laser-generated single bubbles of different sizes were matched with experimental results. The model was subsequently used to simulate the tandem bubble interactions in anti-phase oscillation. The results show that jet shape and volume are predominately controlled by the maximum diameter of the first bubble (D_1) while jet speed is linearly correlated with the maximum diameter of the second bubble (D_2). In comparison, jet momentum and kinetic energy are more sensitive

to variations in bubble size and increase more rapidly with both D_1 and D_2 , especially at large bubble sizes.

Contents

Abstract	iv
List of Tables	viii
List of Figures	ix
Acknowledgements	xiii
1. Introduction	1
2. Materials and Methods.....	4
2.1 Microfluidic Chip	4
2.2 Experimental System for Bubble Generation and High-speed Imaging of Tandem Bubble Interaction.....	8
2.3 Lasers and Optical Setup.....	9
2.4 High-speed Imaging of Bubble Dynamics and Tandem Bubble Interactions	11
3. Model Simulation of Tandem Bubble Interaction	15
3.1 Model Parameters and Assumptions	16
3.2 Governing Equations and Discretization.....	19
3.3 Initial Conditions.....	22
3.2.4 Boundary Conditions.....	23
3.2.5 Time Stepping Strategy	24
4. Results and Discussion.....	25
4.1 Single Bubble Dynamics	25
4.1.1 Experimental Results	25
4.1.2 Calibration of 3DynaFS-BEM Model Parameters	29

4.2 Tandem-Bubble Dynamics.....	34
4.2.1 Comparison between Simulation and Experimental Results.....	34
4.2.2 Jet Speed Comparison.....	38
4.2.3 Analysis of Simulated Jet Parameters.....	45
5. Conclusion and Future Work.....	64
Bibliography	67

List of Tables

Table 1 IMCAON Frame Timing Setup	13
Table 2 Comparison between D_{max} and $D_{(t=2\mu s)}$ for single bubble oscillations shown in Figure 11	28
Table 3 3DynaFS-BEM Parameters Calibration in Figure 14	32
Table 4 Experiments and Simulation Matchup	33

List of Figures

Figure 1 A schematic diagram of the microfluidic chip design layout. Each channel is made of PDMS with a glass bottom. Channel dimension is 25 μm in height and 800 μm in width. Cells are cultured in the 'H' or 'I' patterned area, which is not used in this study. The inter-bubble distance Δ is 40 μm (Yuan, 2013).	5
Figure 2 Schematic diagrams showing the protocols for (a) patterning of micro-sized gold dots on a glass surface using metal lift-off technique and (b) fabrication of PDMS-glass microfluidic chips (Yuan, 2011).....	6
Figure 3 A photograph of the fabricated microfluidic chip with individual channels filled with a blue solution to facilitate visualization [adapted from ref. (Yuan et al., 2011)]......	7
Figure 4 An illustration of the microfluidic channel layout with one pair of gold dots, in which height $H=25\mu\text{m}$, width $W\approx 800\mu\text{m}$, and dots separation distance $\Delta = 40\mu\text{m}$	7
Figure 5 Illustration of the microfluidic channel with a 63 \times objective lens used for focusing two pulsed lasers onto a pair of gold dots for generation of bubble 1 (B_1) and bubble 2 (B_2) [Adapted from ref. (Yuan et al., 2011)].	9
Figure 6 Lasers and optical path in the microscope setup: Laser 1 and 2 are focused by a 63 \times objective on two adjacent focal spots in the microfluidic channel with a separation distance $\Delta = 40\mu\text{m}$ for tandem bubble generation. In addition, a high-speed camera is coupled with the microscope for imaging of bubble dynamics and tandem bubble interaction [adapted from ref. (Sankin et al., 2010)]......	10
Figure 7 A picture of the experimental setup. Red and green lines represent the optical pathways of two pulsed lasers.	11
Figure 8 Timeline of different triggers used in the experiments.....	12
Figure 9 Configuration of a semi-spherical bubble produced in a microfluidic channel.	17
Figure 10 Modeling of a hemi-spherical bubble with an imaging channel	18
Figure 11 High-speed imaging sequences and corresponding time history of bubble diameter for three representative single bubble oscillations. The two vertical lines in (d)-	

(f) indicate the bubble diameters at $t = 2 \mu\text{s}$ and T_m . (a) and (d): $D_{max} = 41 \mu\text{m}$; (b) and (e): $D_{max} = 48.7 \mu\text{m}$; (c) and (f): $D_{max} = 59.2 \mu\text{m}$;	27
Figure 12 Time when a bubble reaches its maximum diameter (T_m) vs. the maximum diameter (D_{max}) for single bubble oscillations.	28
Figure 13 Examples of side view of single bubble simulation at T_m showing the transition from hemi-sphere to cylinder shapes: (a) $D_{max} = 40 \mu\text{m}$; (b) $D_{max} = 50 \mu\text{m}$; (c) $D_{max} = 60 \mu\text{m}$.	29
Figure 14 Examples of 3DynaFS-BEM calibration.	31
Figure 15 Linear fit between $D_{max, e}$ and R_{max}	33
Figure 16 Experiment-Simulation comparison for $D_1 = 40 \mu\text{m}$, $D_2 = 40 \mu\text{m}$ bubble interaction. (a) Experimental results; (b) Simulation results; (c) Superposition of experimental and simulation results.	36
Figure 17 Experiment-Simulation comparison for $D_1 = 40 \mu\text{m}$, $D_2 = 52 \mu\text{m}$ bubble interaction. (a) Experimental results; (b) Simulation results; (c) Superposition of experimental and simulation results.	36
Figure 18 Experiment-Simulation comparison for $D_1 = 56 \mu\text{m}$, $D_2 = 44 \mu\text{m}$ bubble interaction. (a) Experimental results; (b) Simulation results; (c) Superposition of experimental and simulation results.	37
Figure 19 Experiment-Simulation comparison for $D_1 = 56 \mu\text{m}$, $D_2 = 56 \mu\text{m}$ bubble interaction. (a) Experimental results; (b) Simulation results; (c) Superposition of experimental and simulation results.	37
Figure 20 Images of tandem bubbles illustrating the center axis, and proximal end and distal ends of bubble 1.	39
Figure 21 Variation of bubble 1 tip positions for the proximal (in red) and distal (in green) ends with time and the linear fits for determining the touchdown time and the average speed of J_1 .	40
Figure 22 Experimentally measured jet speed vs. D_1 and D_2 . (a) Jet speed vs. D_1 and D_2 ; (b) Jet speed vs. D_1 ; (c) Jet speed vs. D_2 .	41

Figure 23 Examples of jet tip position vs. time, collected with one of the bubble sizes fixed. (a) $D_1 = 44 \mu\text{m}$; (b) $D_1 = 56 \mu\text{m}$; (c) $D_2 = 44 \mu\text{m}$; (d) $D_2 = 56 \mu\text{m}$	43
Figure 24 Correlation between jet speed and maximum bubble sizes (D_1 and D_2). (a) Contour plot of jet speed vs. D_1 and D_2 ; (b) Jet speed vs. D_1 at different D_2 values; (b) Jet speed vs. D_1 at different D_2 values.....	44
Figure 25 Definition of different parameters that are used to describe jet geometry in 3DynaFS-BEM.....	48
Figure 26 Definition of jet geometry parameters.....	49
Figure 27 Jet Shape comparison at touchdown: left corner shows the maximum bubble sizes in the form of D_1 - D_2	51
Figure 28 Correlation between jet volume (V) and jet height (h) at different values of D_1	52
Figure 29 Correlation between jet volume (V) and jet height (h) at different values of D_2	53
Figure 30 Correlation between top view jet parameters' and maximum bubble sizes (D_1 and D_2). (a), (d) and (g) are the 3-D plots of BR - tv , HR - tv and RR - tv 's correlations with D_1 and D_2 ; (b), (e) and (h) are the corresponding images projected along D_2 -axis; (c), (f) and (i) are the corresponding images projected along D_1 -axis.....	55
Figure 31 Correlation between side view jet parameters' and maximum bubble sizes (D_1 and D_2). (a), (d) and (g) are the 3-D plots of BR - sv , HR - sv and RR - sv 's correlations with D_1 and D_2 ; (b), (e) and (h) are the corresponding images projected along D_2 -axis; (c), (f) and (i) are the corresponding images projected along D_1 -axis.....	56
Figure 32 Correlation between maximum jet volume and maximum bubble sizes (D_1 and D_2). (a) Vol_{max} vs. D_1 and D_2 ; (b) Vol_{max} vs. D_1 ; (c) Vol_{max} vs. D_2	57
Figure 33 Correlation between maximum jet height and maximum bubble sizes (D_1 and D_2). (a) h_{max} vs. D_1 and D_2 ; (b) h_{max} vs. D_1 ; (c) h_{max} vs. D_2	58
Figure 34 Correlation between maximum jet base radius and maximum bubble sizes (D_1 and D_2). (a) BR_{max} vs. D_1 and D_2 ; (b) BR_{max} vs. D_1 ; (c) BR_{max} vs. D_2	58

Figure 35 Correlation between maximum jet momentum (M_{max}) and maximum bubble sizes (D_1 and D_2). (a) M_{max} vs. D_1 and D_2 ; (b) M_{max} vs. D_1 ; (c) M_{max} vs. D_2 60

Figure 36 Correlation between maximum jet kinetic energy (KE_{max}) and maximum bubble sizes (D_1 and D_2). (a) KE_{max} vs. D_1 and D_2 ; (b) KE_{max} vs. D_1 ; (c) KE_{max} vs. D_2 60

Figure 37 Correlation between equivalent jet speed from momentum (V_{Mom}) and maximum bubble sizes (D_1 and D_2). (a) V_{Mom} vs. D_1 and D_2 ; (b) V_{Mom} vs. D_1 ; (c) V_{Mom} vs. D_2 62

Figure 38 Correlation between equivalent jet speed from kinetic energy (V_{KE}) and maximum bubble sizes (D_1 and D_2). (a) V_{KE} vs. D_1 and D_2 ; (b) V_{KE} vs. D_1 ; (c) V_{KE} vs. D_2 . .. 62

Acknowledgements

I would like to express my sincere gratitude to the people who have helped and supported me throughout this thesis research. I am grateful to my advisor, Professor Pei Zhong, for his continuous support and inspiration from initial concept inception to experimental design and results analysis. Also, I want to express my gratitude to Professor Edward Shaughnessy and Professor Laurens Howle for their general support and willingness to serve on my thesis committee.

I want to especially acknowledge the support from Dr. Georges Chahine and Dr. Chao-Tsung Hsiao of DYNAFLOW, INC. They have taught me the boundary element method in modeling bubble dynamics and allowed me to use their software 3DynaFS-BEM to carry out the numerical analysis that contributes significantly to this thesis work.

I would like to acknowledge with much appreciation the valuable support from my colleagues at the Therapeutics Research Lab in the Department of Mechanical Engineering and Material Sciences here at Duke University. Dr. Fang Yuan and Dr. Georgy Sankin have taught me the essential skills in working with the experimental system. I want to thank Jaclyn Lautz, Joseph Kleinhenz, Ying Zhang and David Piech for sharing their interesting ideas and experience with me during this thesis research.

Without all these help and encouragement I could not finish this thesis within a short period of time.

Finally, I would like to give special thanks to my parents for their tireless support throughout my college and graduate studies.

1. Introduction

Tandem bubble interaction with jet formation in a microfluidic channel has been shown to provide a unique and versatile technique for site-specific membrane poration with potential applications in targeted drug delivery (Sankin et al., 2010) as well as a new physical method for probing the bioeffects induced by cavitation bubbles at the single cell level (Yuan, 2013). Experiments have shown that single bubble of 50 μm in maximum diameter produced by a 5 ns pulsed laser focused in the microfluidic channel will expand and collapse without jet formation or resultant cell membrane poration. However, by introducing a second bubble in close proximity (40 μm) to the first one after it has reached the maximum expansion, the two bubbles will be set into a coupled, anti-phase oscillation, which leads to asymmetric bubble collapse and formation of two re-entrant jets moving in opposite directions. The associated jetting flow has been found to be critical in the localized and directional membrane poration of individual cells placed nearby (Sankin et al., 2010).

The effect of phase delay between two bubbles with comparable maximum sizes (i.e. 50 μm) has been evaluated previously (Yuan et al., 2011). It was found that the jet speed can be maximized by introducing the second bubble near the maximum expansion of the first bubble, corresponding to an anti-phase oscillation of the tandem bubbles. During the experiment, it was often observed that the maximum bubble size could change up to 10% presumably due to localized variation in laser absorption in the

fluid medium or fluctuations in laser output energy. In addition, varying bubble size may provide a convenient means to modulate the jetting flow and thus resultant shear stress delivered to a target cell without changing its proximity to the tandem bubbles. Despite this potential benefit, the effects of varying bubble sizes on tandem bubble interaction and associated jet formation have not been investigated.

A numerical model based on boundary element method (BEM) has been recently developed to simulate tandem bubble interactions and reasonable agreements with experimental data have been observed (Hsiao et al., 2013). One unique advantage of the numerical model is that much more detailed analysis of the bubble-bubble interaction can be performed, compared to experimental observations using a state-of-the-art ultra high-speed camera, leading to more insights into the physical parameters that can critically influence the tandem bubble interaction and jet formation.

The goal of this thesis therefore is to combine experimental observations with numerical analysis to investigate the effects of bubble size on tandem bubble interaction and jet formation. In chapter 2, the experimental setup is described. In chapter 3, BEM and related principles used in CFD code, 3DynaFS-BEM, is described in detail. In chapter 4, after comparing experimental and simulation results to validate and calibrate the CFD code, several jet parameters are extracted from the simulation output to explore the dependence of jet formation on maximum bubble sizes. In chapter 5, conclusions

regarding the dependence of jet formation on bubble sizes are drawn based on the results of chapter 4 and recommendations for future work are given.

2. Materials and Methods

In this chapter the experiment setup used to capture and analyze the interaction of tandem bubbles and associated jet formation in a microfluidic channel is described.

The experimental setup consists of three components: 1) a microfluidic chip with micro-channels decorated by micron-sized gold dots on their glass substrate, 2) two 5 ns pulsed Nd: YAG lasers for tandem bubble generation, and 3) an inverted microscope equipped with an ultra high-speed camera for observing the transient tandem bubble interaction and jet formation.

2.1 Microfluidic Chip

The microfluidic channel used for tandem bubble generation was designed and fabricated following an established protocol (Yuan et al., 2011). The detailed layout of the patterns inside each channel for bubble generation and cell attachment is shown in Figure 1. Briefly, three channels of 25 mm in nominal length were constructed in parallel with inlet and outlet ports connected to both ends of the channels to facilitate injection and exchange of different fluid media. Each channel, with a dimension of 800 μm by 25 μm in width and height, contains 10 sets of gold-dot pairs at a fixed inter-bubble distance ($\Delta = 40 \mu\text{m}$) that are used for bubble generation. In addition, the 'H' or 'I' pattern in each set was a $32 \times 32 (\mu\text{m}^2)$ area that could be covered with fibronectin for cell culture to control the location, shape and adhesion pattern of individual cells to be treated by tandem bubbles.

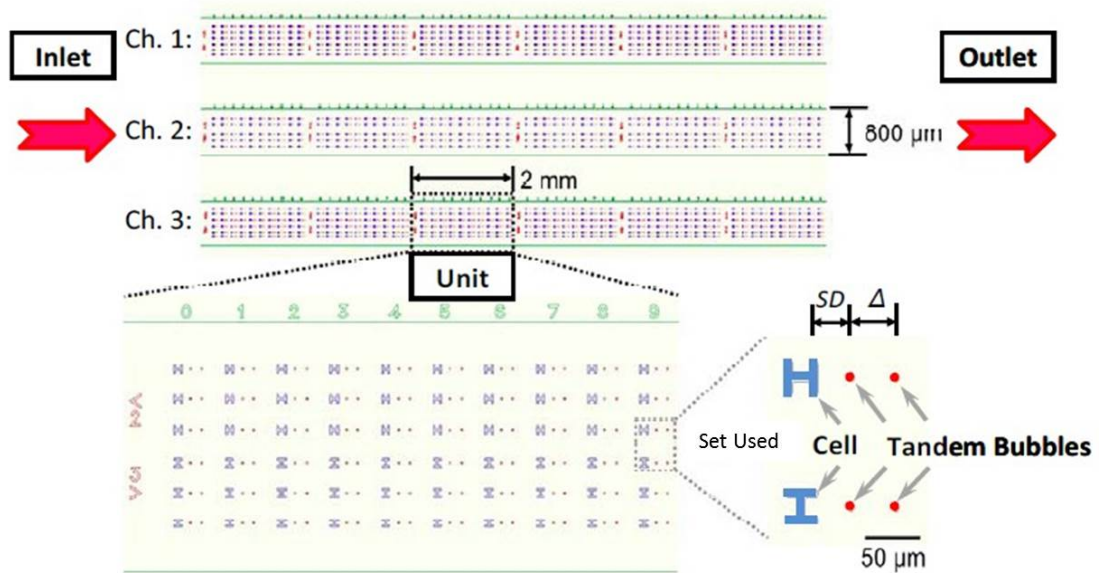


Figure 1 A schematic diagram of the microfluidic chip design layout. Each channel is made of PDMS with a glass bottom. Channel dimension is 25 μm in height and 800 μm in width. Cells are cultured in the 'H' or 'I' patterned area, which is not used in this study. The inter-bubble distance Δ is 40 μm (Yuan, 2013).

The general procedures employed in the micro-chip fabrication are shown in Figure 2. First, a thin layer of photoresist (NFR 015, JSA Micro.) was spin-coated on a 1-mm thick microscopic glass slide (#48300, VWR International). Second, a chrome master photomask (Photo Sciences) with designed patterns (as shown in Figure 1) was used to perform photolithography on the coated layer of photoresist using a lithography mask aligner (MA6/BA6, Karl Suss). Third, an array of paired gold dots of 15 nm thick and 6 μm in diameter was deposited on the glass surface using an electron beam evaporator (PVD 75, Kurt Lesker) preceded by a 2-nm thick chrome underlayer deposition in order

to enhance the adhesion between the glass surface and the gold dots. The 6- μm diameter was selected to ensure sufficient area for laser absorption while providing a small enough target ($<$ the focal spot of the laser beam) for easy alignment and consistency in bubble generation.

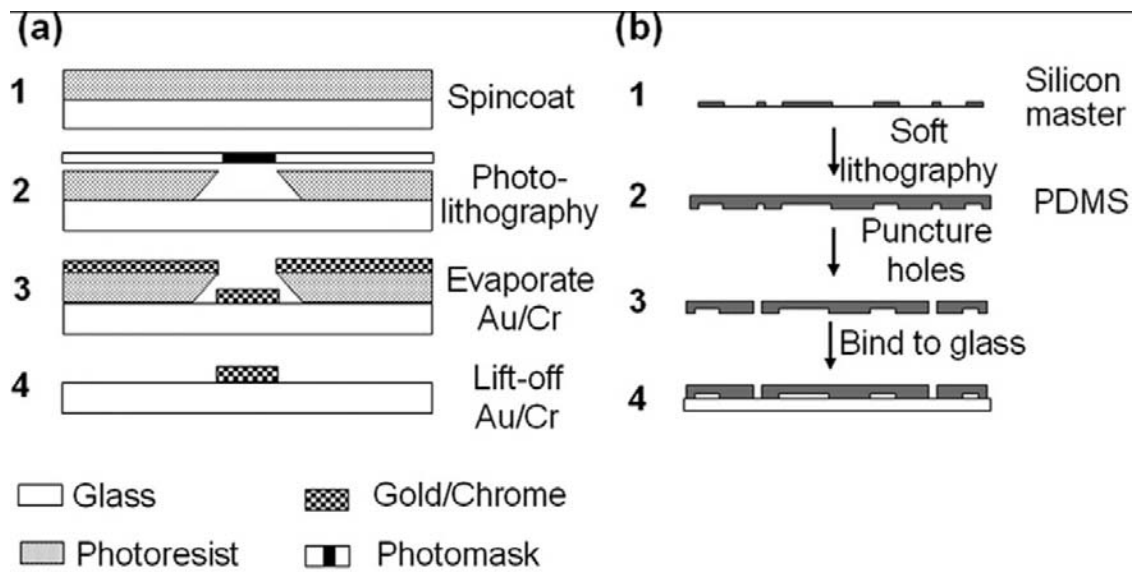


Figure 2 Schematic diagrams showing the protocols for (a) patterning of micro-sized gold dots on a glass surface using metal lift-off technique and (b) fabrication of PDMS-glass microfluidic chips (Yuan, 2011).

The channel was filled with deionized water, which had similar density, surface tension, and viscosity to the cell culture medium used in bioeffect studies. An example of the fabricated microfluidic chip is shown in Figure 3.

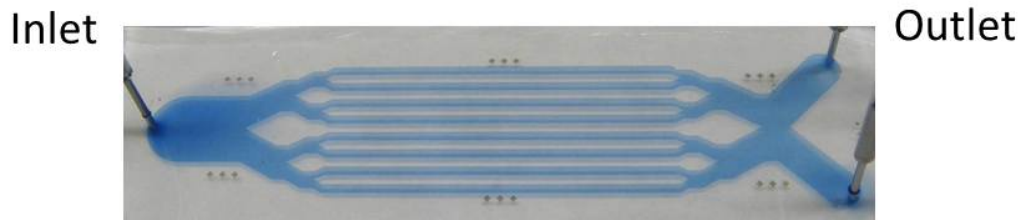


Figure 3 A photograph of the fabricated microfluidic chip with individual channels filled with a blue solution to facilitate visualization [adapted from ref. (Yuan et al., 2011)].

For each test, one pair of the gold dots in the middle two lines of the pattern was used for bubble generation to ensure consistency in experimental results. Figure 4 shows a sketch of one pair of gold dots inside a channel, the width W is approximated by the channel width (i.e., $800\ \mu\text{m}$) and the channel height is $H = 25\ \mu\text{m}$.



Figure 4 An illustration of the microfluidic channel layout with one pair of gold dots, in which height $H=25\ \mu\text{m}$, width $W\approx 800\ \mu\text{m}$, and dots separation distance $\Delta = 40\ \mu\text{m}$.

2.2 Experimental System for Bubble Generation and High-speed Imaging of Tandem Bubble Interaction

The fabricated microfluidic chip was placed on the stage of an experimental system constructed from an inverted microscope (Axio Observer D1, Zeiss), which has been described in detail previously (Sankin et al., 2010). As shown in Figure 5, a 63x objective lens placed on the bottom side of the microfluidic channel, was used to focus two 5 ns pulsed lasers onto a pair of gold dots inside the channel for tandem bubble generation. Each laser pulse was strongly absorbed by the target gold dot, leading to a rapid localized heating and vaporization of the surrounding fluid medium and consequently the formation of a bubble (Yuan et al., 2011). The dynamics of bubble oscillation and tandem bubble interaction inside the channel were captured through the same objective lens using a high-speed camera connected to the microscope (see Figure 6). A picture of the experimental setup including the inverted microscope and two pulsed lasers is shown in Figure 7 (Yuan et al., 2013).

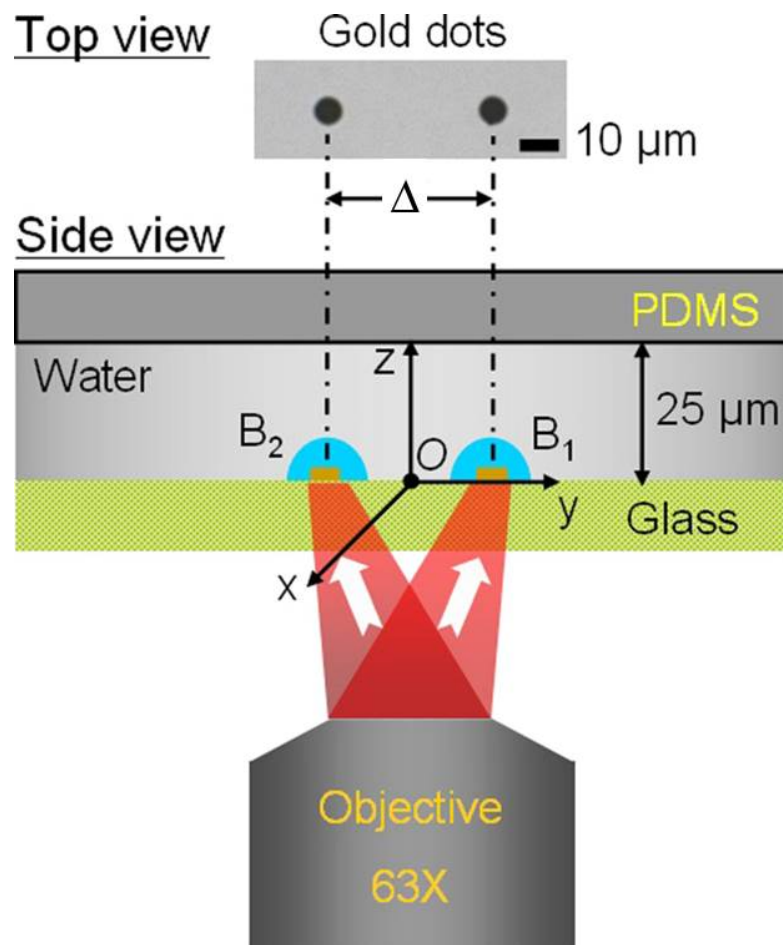


Figure 5 Illustration of the microfluidic channel with a $63\times$ objective lens used for focusing two pulsed lasers onto a pair of gold dots for generation of bubble 1 (B_1) and bubble 2 (B_2) [Adapted from ref. (Yuan et al., 2011)].

2.3 Lasers and Optical Setup

Two Q-switched Nd: YAG pulsed lasers (Laser 1: Minilase I; Laser 2: Solo PIV, New Wave Research) with $532\ \text{nm}$ in wavelength and $5\ \text{ns}$ pulse duration, were used for tandem bubble generation. Each laser beam can be steered individually through a set of mirrors and focused through the $63\times$ objective lens onto a gold dot inside the

microfluidic channel (see Figure 6 and 7). Alignment of the two pulsed lasers with a pair of gold dots was facilitated by the x-y position stage of the microscope together with a rotating slide holder (Yuan et al., 2011).

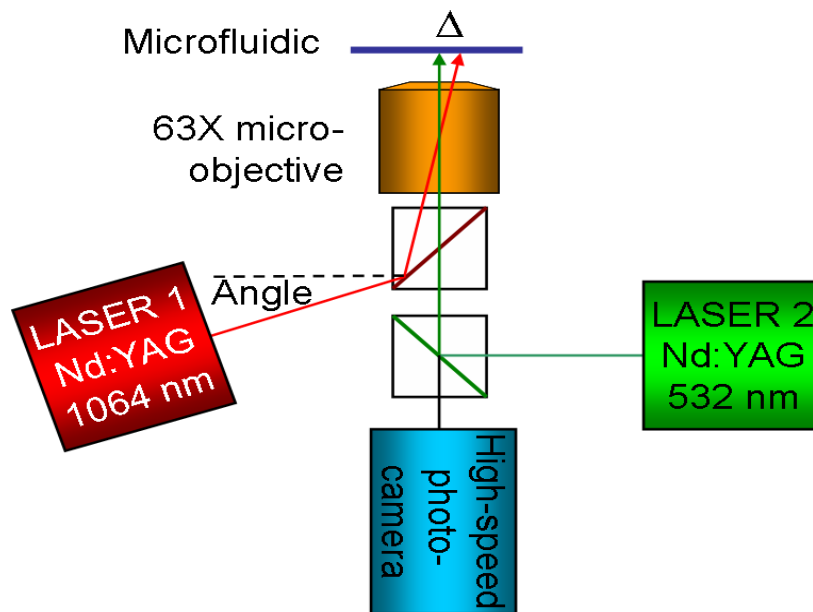


Figure 6 Lasers and optical path in the microscope setup: Laser 1 and 2 are focused by a 63×objective on two adjacent focal spots in the microfluidic channel with a separation distance $\Delta = 40 \mu\text{m}$ for tandem bubble generation. In addition, a high-speed camera is coupled with the microscope for imaging of bubble dynamics and tandem bubble interaction [adapted from ref. (Sankin et al., 2010)].

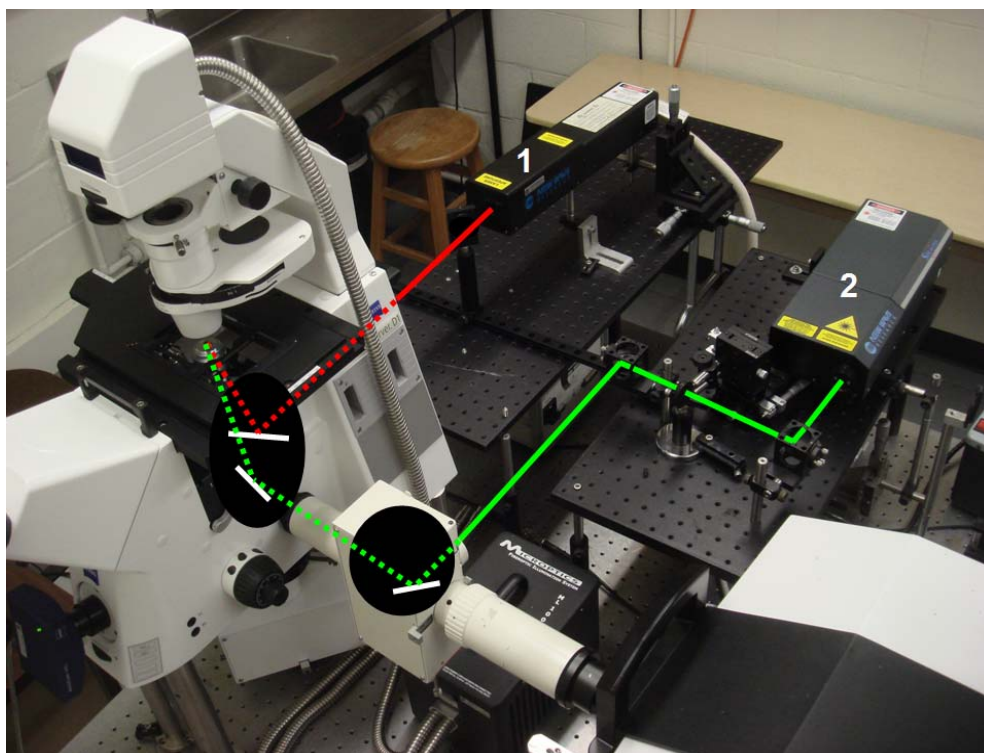


Figure 7 A picture of the experimental setup. Red and green lines represent the optical pathways of two pulsed lasers.

2.4 High-speed Imaging of Bubble Dynamics and Tandem Bubble Interactions

The dynamics of laser-generated bubble interaction in the microfluidic channel was captured using a high-speed camera (IMACON 200, DRS Handland) operated at 50 ns exposure time and a framing rate of 1~10 million frames/second. A fiber-optic coupled Xenon flash with 200 μ s pulse duration (ML 1000, Dyna-Lite) was used to provide backlight illumination for the high-speed camera.

A digital delay generator (BNC 555, Berkeley Neclonics Coporation) was used to control precisely the timing of triggers to individual lamps of the two lasers, Q-switch (for laser pulse firing), and the high-speed camera. Figure 8 shows the timeline for the release of different triggers in the experiment. Typically, the moment when the backlight flash lamp was fired was used as the starting point of the experiment. The lamps of laser 1 and laser 2 were triggered at 25 μ s and 60 μ s, respectively, to arm the lasers. The trigger (Q-switch) to fire laser 1 was released at 120 μ s and laser 2 was fired at 122 μ s, leading to the production of tandem bubbles with an inter-bubble delay of 2 μ s. This ensures approximately the production of an anti-phase tandem bubble interaction (see Chapter 4).

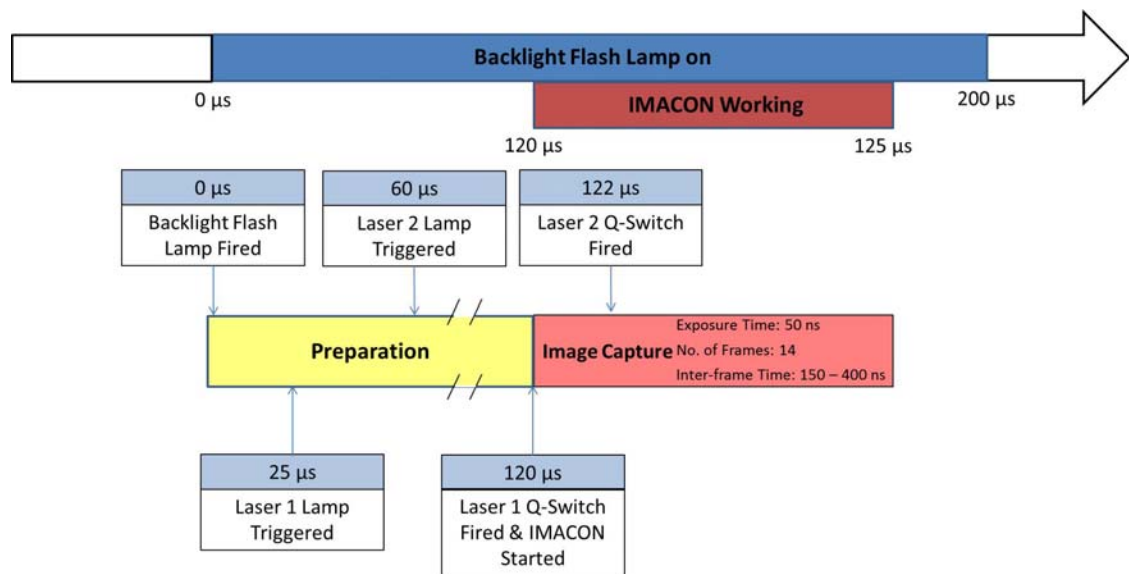


Figure 8 Timeline of different triggers used in the experiments

The high-speed camera (IMACON 200, DRS Handland) can take a maximum of 14 frames in each imaging sequence. For high-speed imaging, the moment when laser 1 was triggered (120 μs in Figure 8 timeline) was considered as the starting point (0 μs) in “Image Capture”. Table 1 summarizes the timing setup used for the high-speed camera. The inter-frame time was uneven and adjusted to ensure that there were enough frames to capture the maximum sizes of both bubbles (D_1 and D_2), as well as the dynamic process of the jet formation.

The outputs of IMACON camera are images in “.tiff” format, which were used to measure the bubble sizes (D_1 and D_2) with the software with IMACON camera, and then stored for backup. Such outputs were converted to “.jpg” format to be opened in Windows Paint for the measurement of tip positions in pixels. Then with a conversion, jet tip positions were calculated.

Table 1 IMCAON Frame Timing Setup

Frame No.	Frame Timing (μs)
1	1.75
2	1.9
3	2.05
4	2.2
5	2.35
6	2.5
7	2.65
8	2.8
9	2.95
10	3.2

11	3.6
12	4
13	4.4
14	4.8

3. Model Simulation of Tandem Bubble Interaction

3DynaFS-BEM is a software package for Computational Fluid Dynamics (CFD), developed by Dr. G. Chahine and Dr. C. Hsiao of DYNAFLOW, INC. especially for simulating single and multiple bubbles dynamics and their interactions.

In this study, 3DynaFS-BEM was used as a simulation tool for the analysis of bubble dynamics and tandem bubble interaction because of its efficiency with reasonable accuracy in capturing the asymmetric bubble deformation and jet formation during tandem bubble interaction (Hsiao et al., 2013). A general review of boundary element method (BEM) and its applications in modeling of bubble dynamics can be found in (Blake and Gibson, 1987).

In the experiments, individual bubbles were created on the glass substrate of a microfluidic channel, and expanded initially in a semispherical form, as shown in Figure 9. To simulate the boundary condition on the glass substrate (bottom, $z = 0$), an image channel was introduced in the 3DynaFS-BEM code (Figure 10) so that a “complete” bubble formed by the real bubble at the boundary with its mirror image could be modeled. Moreover, the confinement of a single or tandem bubble in the microfluidic channel was simulated by two parallel disks, which has been found to generate reasonable simulation results in comparison with experimental observations (Hsiao et al., 2013).

3.1 Model Parameters and Assumptions

The flow around a single or tandem bubble is assumed to be irrotational during the period of bubble deformation before jet penetration through the bubble wall, so that a velocity potential ϕ can be introduced that satisfies:

$$\vec{u} = \nabla \phi \quad (3.1)$$

where $\vec{u} = (u, v, w)$ is the velocity vector of the fluid flow. Further, the flow is assumed to be incompressible, leading to the Laplace's equation for ϕ :

$$\nabla^2 \phi = 0 \quad (3.2)$$

Considering the solid-wall (i.e., glass substrate) boundary condition at the bottom of the microfluidic channel, the velocity component in z direction must be 0 and should satisfy the following equation:

$$u(x, y, 0) = \left. \frac{\partial \phi}{\partial z} \right|_{z=0} = 0 \quad (3.3)$$

This boundary condition can be ensured by specifying the velocity potential ϕ in the image channel (see Figure 11) to be given by:

$$\phi(x, y, z) = \phi(x, y, -z), \text{ at } z < 0 \quad (3.4)$$

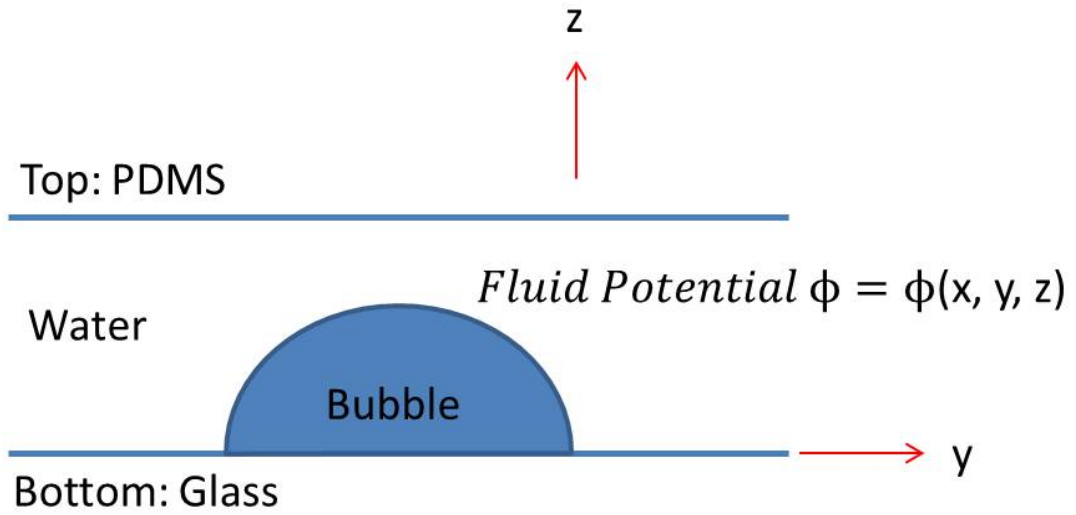


Figure 9 Configuration of a semi-spherical bubble produced in a microfluidic channel

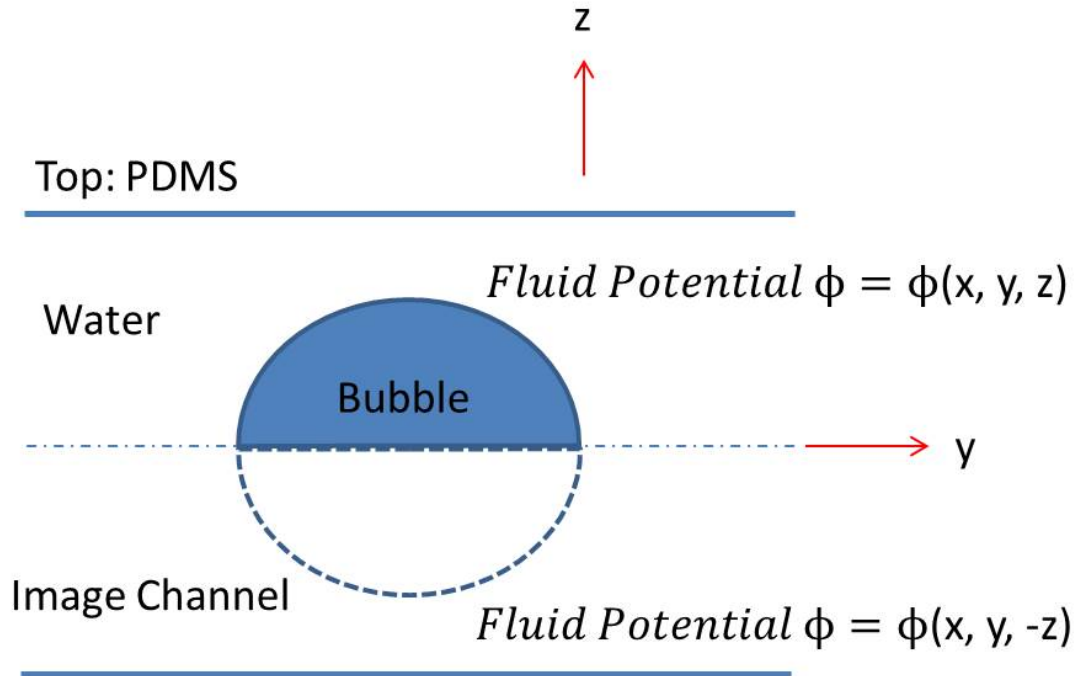


Figure 10 Modeling of a hemi-spherical bubble with an imaging channel

In single bubble simulations, the bubble was assumed to start from its minimum size in a spherical shape with a radius of $R_0 = 2\mu\text{m}$, which was small enough compared with its distance to boundaries, so that the bubble was considered to undergo an unbounded expansion during the initial stages of bubble growth. Vaporization of the liquid was assumed to occur at a rate fast enough so that the vapor pressure inside the bubble remained equal to the equilibrium vapor pressure at the ambient temperature. Moreover, all the solid boundaries were assumed to be non-deformable. Gravity was neglected and the ambient pressure was assumed to be constant (i.e., $P_{amb}=101,235\text{Pa}$).

The gas inside the bubble was assumed to experience a polytropic process with a constant polytropic index k such that:

$$P_g R^{3k} = P_{g0} R_0^{3k} \quad (3.5)$$

where P_g is gas and vapor pressure, R is bubble radius at time t , P_{g0} is gas and vapor pressure, R_0 is bubble radius at initial time $t = 0$.

In tandem bubble simulations, the two bubbles were placed symmetrically about the disk center in x-y plane. This rendered each bubble to undergo an asymmetrical collapse if they existed individually. Such asymmetry would lead to a small jet along the line connecting the two bubble centers. In this study, jetting effect from tandem bubble interaction was assumed strong enough to dominate over this asymmetry effect.

3.2 Governing Equations and Discretization

In this section, the governing equation derived from the Laplace's equation in (3.2) and its discretization into matrix form for CFD computation are introduced, largely following the presentation in ref. (Hsiao et al., 2013). The Laplace's equation can be solved by the BEM using an integral solution based on the Divergence Theorem in 3-D fluid,

$$\iiint_V (\phi \nabla^2 G - G \nabla^2 \phi) dV = \iint_S \hat{n} \cdot [\phi \nabla G - G \nabla \phi] dS \quad (3.6)$$

where V denotes the 3-D domain of fluid body, and S is the surface of V , with \hat{n} being the unit normal vector pointing outward.

The velocity potential ϕ is harmonic in the fluid domain and G is the Green's function, which can also be selected to be harmonic everywhere except for some discrete points using the form:

$$G = -\frac{1}{|\vec{x} - \vec{y}|} \quad (3.7)$$

where \vec{x} is the coordinate of a fixed point of interest in V , and \vec{y} is a point on the boundary surface S .

Equation (3.6) reduces to Green's formula with a being the solid angle at \vec{x} under which the domain V is seen.

$$a\phi(\vec{x}) = \iint_S \hat{n}_y \cdot [\phi(\vec{y})\nabla G(\vec{x}, \vec{y}) - G(\vec{x}, \vec{y})\nabla\phi(\vec{y})]dS \quad (3.8)$$

$$a \begin{cases} = 4\pi, & \text{if } \vec{x} \text{ is in the fluid} \\ = 2\pi, & \text{if } \vec{x} \text{ is on a smooth surface} \\ < 4\pi, & \text{if } \vec{x} \text{ is at a sharp corner} \end{cases}$$

Equation (3.8) can be solved using BEM numerically by discretizing all the boundaries into either triangles or quadrilateral panels S_k . In this study, only triangular panels were used, in which all the quantities are assumed to vary linearly. Using this method, equation (3.8) can be written in a discretized form:

$$a\pi\phi(\vec{x}) = \sum_{k=1}^P \iint_{S_k} [\phi(\vec{y}) \frac{\partial G(\vec{x}, \vec{y})}{\partial \hat{n}_y} - G(\vec{x}, \vec{y}) \frac{\partial \phi(\vec{y})}{\partial \hat{n}_y}] dS_k \quad (3.9)$$

where P is the number of surface panels on the boundary. To evaluate the integrals over

S_k , given in (3.9), it was assumed that ϕ and $\frac{\partial \phi}{\partial \hat{n}}$ vary linearly over a panel and thus

could be described by the values at the panel nodes as:

$$a\pi\phi_j = \sum_{k=1}^P \sum_i^m [B_i^k \phi_i^k - A_i^k (\frac{\partial \phi}{\partial \hat{n}})_i^k], \quad j = 1, 2, \dots, N \quad (3.10)$$

where ϕ_i^k and $(\frac{\partial \phi}{\partial \hat{n}})_i^k$ are the potential and its normal derivative at node i of panel k .

A_i^k and B_i^k are influence coefficients obtained from elementary integrations (Miller 1987). N is the total number of nodes, P is the total number of panels and constant m is set to be 3 as the mesh is discretized into triangular elements.

Collecting the contributions from the same node and summing up, (3.10) could be rewritten in a condensed matrix form:

$$\bar{A} \frac{\partial \phi}{\partial \hat{n}} = (-a\pi I + \bar{B})\phi \quad (3.11)$$

where I is the $N \times N$ identity matrix, and \bar{A} and \bar{B} are $N \times N$ coefficient matrices collected from A_i^k and B_i^k , respectively.

3.3 Initial Conditions

The bubble was assumed to grow from a small spherical bubble originated at the boundary of the water-image channel during the initial stage of bubble expansion, which can be described by the Rayleigh-Plesset equation:

$$\rho[R\ddot{R} + \frac{3}{2}\dot{R}^2] = P_{g0}\left(\frac{R_0}{R}\right)^{3k} + P_v - P_{amb} - \frac{2\sigma}{R} \quad (3.12)$$

where $R(t)$ is the bubble radius at time t , ρ is the liquid density, and σ is the surface tension coefficient. A dot over a symbol represents differentiation with respect to time. P_v is the liquid vapor pressure at the ambient temperature, and P_{g0} represents the partial pressure of the gas inside the bubble at initial radius, R_0 .

In this work, k was set to be 1.25 to ensure a good match between simulation and experimental results in bubble expansion. It has been shown that integral of equation (3.12) gives (Brennen, 1995):

$$\dot{R} = \sqrt{\frac{2}{\rho} \left[\frac{P_g}{3(1-k)} (1 - \alpha^{3k-3}) + \frac{P_v - P_a}{3} (1 - \alpha^{-3}) - \frac{\sigma}{R} (1 - \alpha^{-2}) \right]^{1/2}} \quad (3.13)$$

where $\alpha = R(t) / R_{\max}$, and R_{\max} is the maximum radius the bubble produced in a free field. Such bubbles would be used to simulate the bubble dynamics generated in experimental microfluidic channel by laser irradiation.

3.2.4 Boundary Conditions

At a point X_s on any boundary S_B , the boundary condition includes the continuity in velocity at fluid-solid and fluid-gas interface normal direction:

$$\nabla \phi \cdot \hat{n} = \vec{u}_s \quad (3.14)$$

where \vec{u}_s is the boundary velocity and \hat{n} is the local unit normal to the boundary.

Specially, for a point at fluid-solid interface,

$$\nabla \phi \cdot \hat{n} = 0 \quad (3.15)$$

The material derivative of velocity potential is defined by:

$$\frac{D\phi}{Dt} = \frac{\partial \phi}{\partial t} + \vec{u} \cdot \nabla \phi \quad (3.16)$$

In this work, the fluid at fluid-gas interfaces was treated in a Lagrangian fashion, where the nodes and potential were advanced following (3.16) and (3.17):

$$\frac{D\vec{x}}{Dt} = \vec{u} \quad (3.17)$$

where \vec{x} is the coordinate of a node.

Using the Bernoulli's equation of potential flow and a balance of pressures condition at the surface, the advance of fluid potential on boundaries can be obtained as follows:

$$\frac{D\phi}{Dt} = \frac{1}{\rho} [p_\infty - p_v - p_{g0} \left(\frac{V_0}{V(t)}\right)^k + \sigma C] + \frac{1}{2} |\nabla \phi|^2 \quad (3.18)$$

3.2.5 Time Stepping Strategy

In 3DynaFS-BEM, a simple Euler stepping scheme was used to integrate (3.18) numerically. The value of a prescribed quantity q at time $t + \delta t$ was obtained from its known values at time t as:

$$q(t + \delta t) = q(t) + \frac{dq}{dt}(t)\delta t \quad (3.19)$$

The time step was determined as:

$$\delta t = \frac{\Delta l_{\min}}{25V_{\max}} T_f \quad (3.20)$$

where Δl_{\min} is the minimum distance between the nodes, V_{\max} is the maximum of all computed nodal velocities, and T_f is a prescribed time factor that can be used to control time steps.

To prevent excessively small or large steps leading to inordinately long run times or erroneous results, lower and upper bounds were added to the time steps, rendering the real time step as:

$$\Delta t = \max(\Delta t_{\min}, \min(\delta t, \Delta t_{\max})) \quad (3.21)$$

where Δt_{\min} and Δt_{\max} are the lower and upper bounds prescribed to the program.

4. Results and Discussion

In this chapter, model simulation of a single bubble produced by laser irradiation on a glass surface coated with gold dots was first carried out using the 3DynaFS-BEM code. The key parameters of the model, i.e., the maximum radius of the bubble in free field (R_{max}) and disk size (R_{disk}), were calibrated by comparison with experimental results from single bubbles. Thereafter, the model was used to simulate anti-phase tandem bubble interactions with different bubble sizes. The calculation results were compared with experimental observations regarding the formation and dynamics of jets produced by the tandem bubble interaction.

4.1 Single Bubble Dynamics

Experimentally, the dynamics of single bubble oscillation were captured by the IMACON camera from which the time history of the bubble diameter was determined. In parallel, model simulations were carried out for different sets of R_{max} and R_{disk} , and the results were compared with experimental observations, from which the best match of these parameters were identified for model calibration.

4.1.1 Experimental Results

Figure 11 shows three representative examples of the high-speed imaging sequences (from the top view) and corresponding time history of bubble diameter for

laser-generated single bubble oscillation. In general, following the laser irradiation on a gold dot, a single bubble is created that expands to a maximum size (D_{max}), in about 2 μs and then collapses gradually to a minimum size in and 1.5 to 4 μs . As D_{max} increases from 40 μm to 60 μm , the bubble expansion time becomes longer, and the corresponding collapse time of the bubble lengthens further. As shown in Figure 12, when D_{max} is in the range of 40 μm to 49 μm , T_m , which corresponds to the time when a bubble reaches its maximum size, increases almost linearly with D_{max} . This observation is consistent with the finding from a previous study on single bubble dynamics in microfluidic channels of varying heights (Quinto-Su et al., 2009). In this size range, the bubble is likely in a hemispherical shape during its initial expansion and the constraining effect of the PDMS channel (with a fixed height of 25 μm) on bubble expansion is minimal. In contrast, when D_{max} is in the range of 49 to 60 μm , T_m remains nearly as a constant (i.e., 2.2 μs). Since the maximum bubble radius has reached or exceeded the channel height in this domain, the expansion of the bubble is likely to be constrained by the PDMS channel, leading to a transformation of the bubble shape from hemi-spherical to cylindrical seen along the x-axis (from the side view). This speculation has been confirmed by model simulation (see Figure 13). Overall, for the range of bubble size investigated in this work, the value of T_m only varies slightly from 1.8 to 2.2 μs . Furthermore, as shown in Figure 12 and summarized in Table 2, the difference between D_{max} and bubble diameter at 2 μs after laser irradiates, $D_{(t=2\mu\text{s})}$ is less than 1.5%. Therefore, a delay time of 2 μs was used in

both experiments and model simulations to ensure that anti-phase tandem bubble interactions were produced.

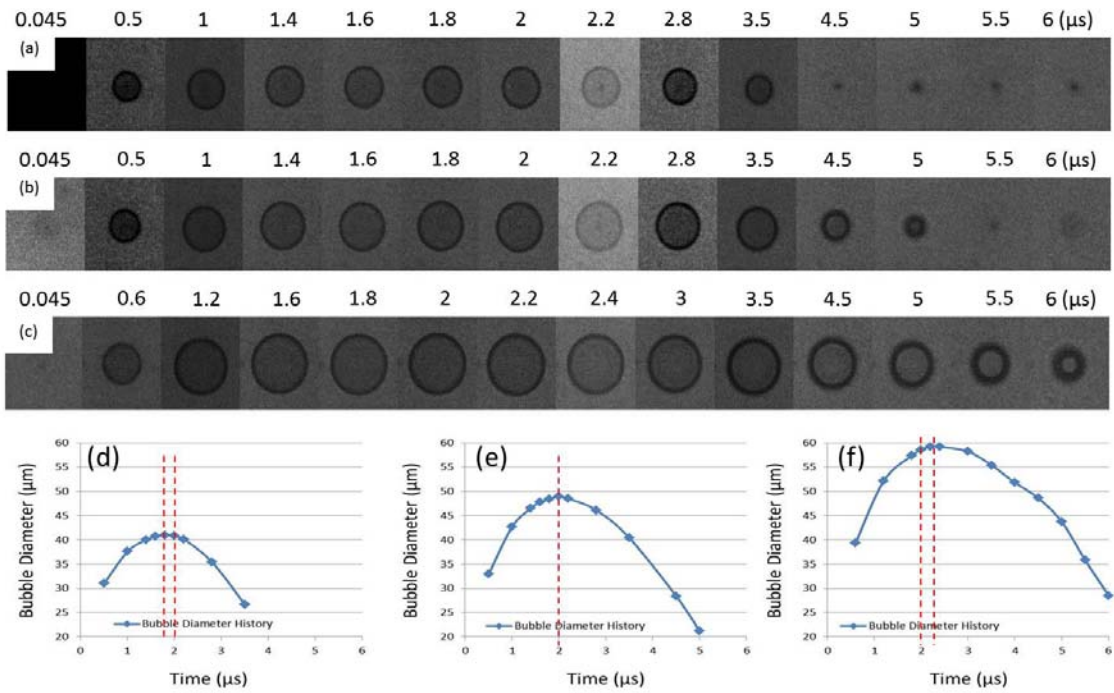


Figure 11 High-speed imaging sequences and corresponding time history of bubble diameter for three representative single bubble oscillations. The two vertical lines in (d)-(f) indicate the bubble diameters at $t = 2 \mu\text{s}$ and T_m . (a) and (d): $D_{max} = 41 \mu\text{m}$; (b) and (e): $D_{max} = 48.7 \mu\text{m}$; (c) and (f): $D_{max} = 59.2 \mu\text{m}$;

Table 2 Comparison between D_{max} and $D_{(t=2\mu s)}$ for single bubble oscillations shown in Figure 11

Figure 11 Subsection	D_{max} (μm)	T_m (μs)	$D_{(t=2\mu s)}$ (μm)	$\frac{D_{max} - D_{(t=2\mu s)}}{D_{max}} \times 100\%$
(a) and (d)	41	1.8	40.8	0.5%
(b) and (e)	48.7	2	48.7	0
(c) and (f)	59.2	2.2	58.6	1.0%

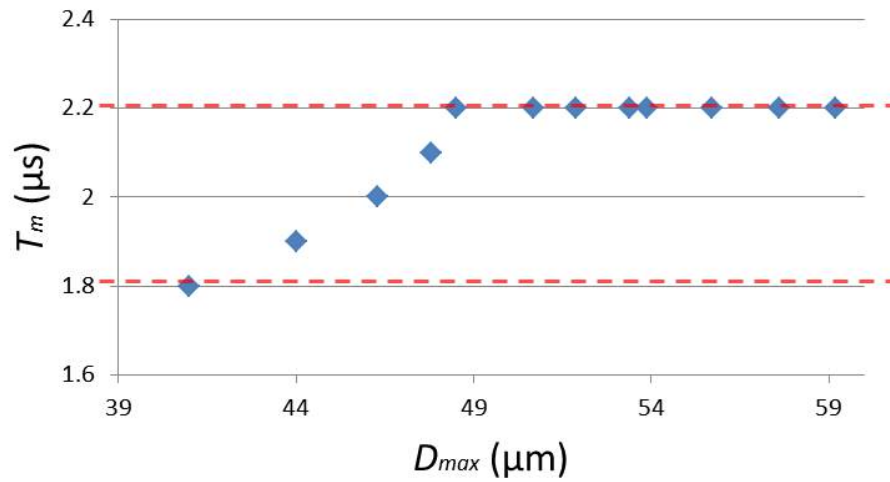


Figure 12 Time when a bubble reaches its maximum diameter (T_m) vs. the maximum diameter (D_{max}) for single bubble oscillations.

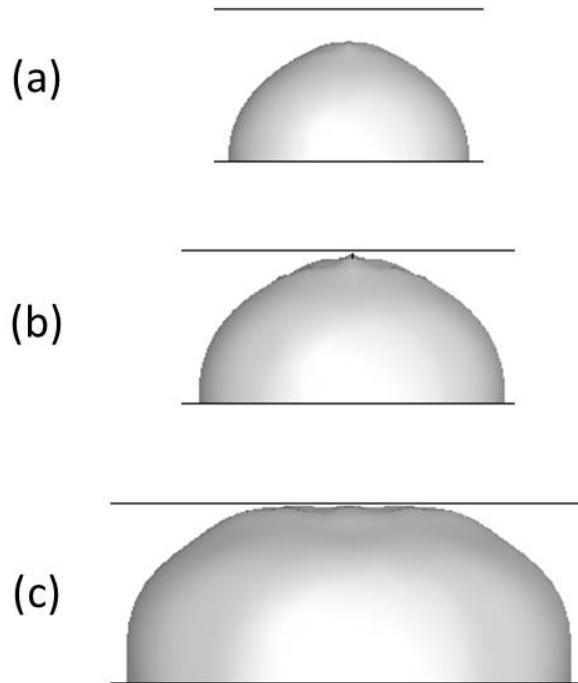


Figure 13 Examples of side view of single bubble simulation at T_m showing the transition from hemi-sphere to cylinder shapes: (a) $D_{max} = 40 \mu\text{m}$; (b) $D_{max} = 50 \mu\text{m}$; (c) $D_{max} = 60 \mu\text{m}$.

4.1.2 Calibration of 3DynaFS-BEM Model Parameters

In the 3DynaFS-BEM code, the initial bubble radius (R_0) and the ambient pressure (p_{amb}) are kept constant. The initial gas pressure inside the bubble (p_{g0}) can be adjusted to vary the maximum bubble radius produced in free field (R_{max}) in a one-to-one correspondence. In addition to p_{g0} and thus R_{max} , the radius of the disk (R_{disk}) that is

used to mimic the boundary can be changed to adjust bubble oscillation period and also influence the maximum bubble size (Hsiao et al., 2013).

We define the “projected radius” R_{proj} as the bubble radius measured from the top view in both experimental and simulation results. Thus, the maximum of $R_{proj} = D_{max}/2$. In this section, an extra subscript “e” or “m” is used to differentiate the same parameters between “experiment” and “model” calculation results. For instance, $D_{max, e}$ and $D_{max, m}$ denote the maximum bubble diameters obtained from experiments and model simulations, respectively.

Three examples of 3DynaFS-BEM parameter calibration are shown in Figure 13. First, we identified the best R_{max} to match between $D_{max, e}$ and $D_{max, m}$. Second, with this R_{max} , simulations of the single bubble oscillation with different sets of R_{disk} were carried out. The best match of R_{disk} values was found to be always between 70 and 80 μm when $D_{max, e}$ was in the range of 40 to 60 μm . To better match the expansion phase of bubble dynamics and $D_{max, m}$, R_{disk} was finally set to be 80 μm for tandem bubble simulations. It can be seen in Figure 13 that when $R_{disk} = 80 \mu\text{m}$, the curve of time history of bubble sizes obtained from 3DynaFS-BEM modeling mostly matched the experimental curves from the aspects of expanding trends and maximum sizes, except that the modeled bubbles expanded a little slower than the experimental ones and collapsed faster.

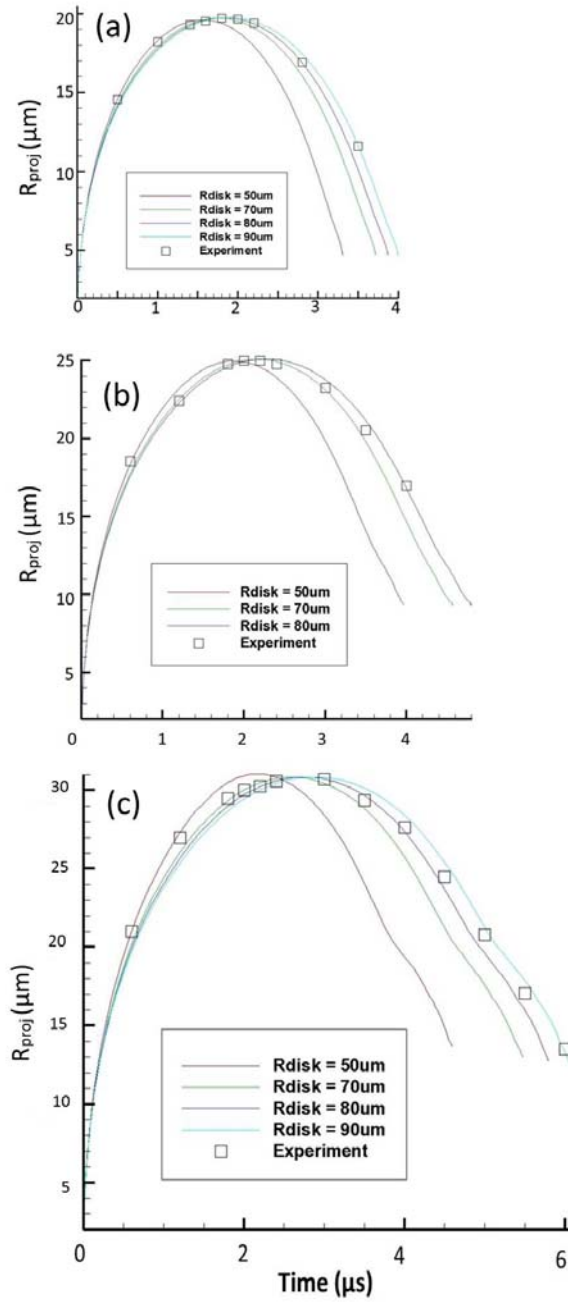


Figure 14 Examples of 3DynaFS-BEM calibration

Table 3 summarizes the values for the best match between $D_{max, e}$, extracted from experimental data in Figure 14 and the corresponding values of $D_{max, m}$ from the model

calculations, together with the two key parameters $R_{max, m}$ and R_{disk} . In all cases, $R_{disk} = 80$ μm .

Table 3 3DynaFS-BEM Parameters Calibration in Figure 14

Figure 14 Subsection	$D_{max, e}$ (μm)	$D_{max, m}$ (μm)	R_{max} (μm)	R_{disk} (μm)
(a)	39.5	39.5	20	80
(b)	50.2	50.3	25	80
(c)	61.7	61.6	30	80

As shown in Figure 15, a linear fit was made between $D_{max, m}$ and one of the two critical parameters from 3DynaFS-BEM code R_{max} , which gives:

$$R_{max} = 0.4157D_{max, e} + 3.9654 \quad (4.1)$$

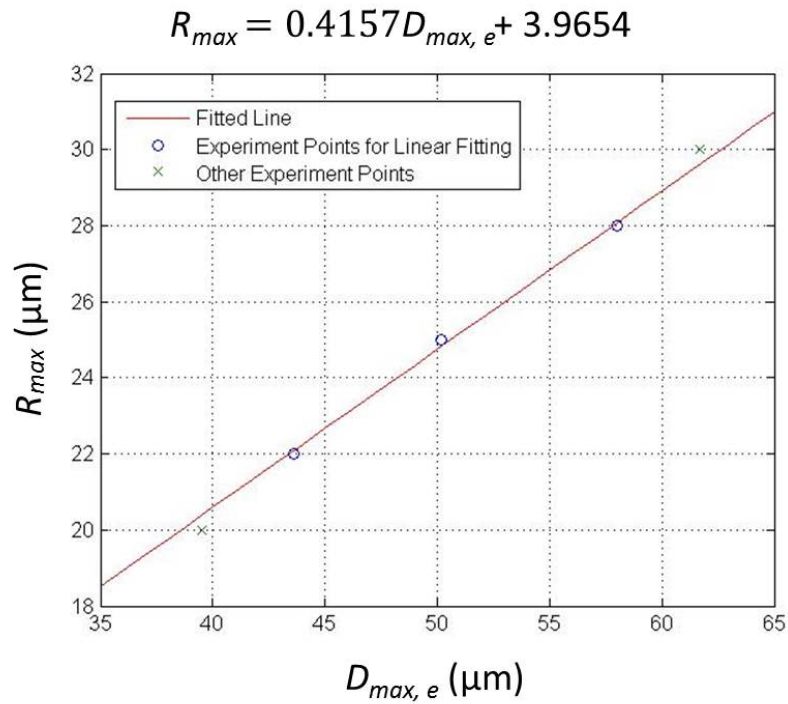


Figure 15 Linear fit between $D_{max,e}$ and R_{max}

In this study, six different values of $D_{max,m}$ were used to cover the full range of bubble sizes in the range of 40 to 60 μm . Table 4 lists the $D_{max,e}$ and the corresponding R_{max} values used in this study (with $R_{disk} = 80 \mu\text{m}$).

Table 4 Experiments and Simulation Matchup

$D_{max,e}$ (μm)	R_{max} (μm)
40	20.19
44	22.19

48	24.05
52	25.74
56	27.29
60	28.67

4.2 Tandem-Bubble Dynamics

Previous studies have shown that the jetting flow produced by tandem bubble interaction plays a vital role in the sonoporation and bioeffects induced in individual cells placed nearby (Sankin et al., 2010).

To gain a better understanding of the tandem bubble interaction and the critical bubble parameters that influence jet formation, model simulations of the tandem bubble interaction have been carried out using different bubble sizes under the condition of anti-phase oscillation. In particular, we will focus on the first jet (J_1) produced by the asymmetric collapse of bubble 1 (B_1) during the tandem bubble interaction, which is more reproducible and often used for cell treatment (Yuan, 2013).

4.2.1 Comparison between Simulation and Experimental Results

Four cases of comparison between experimental and simulation results are shown in Figure 16-19, covering a wide range of bubble size variations. In each figure,

the first row shows the high-speed images of tandem bubble interaction captured by the IMACON camera. The second row shows the corresponding model simulations obtained from 3DynaFS-BEM. The third row is the superposition of the experiment and simulation results for ease of comparison.

Overall, from the top view, the simulation results were found to capture the main features of the tandem bubble interaction in the shape developments of both B_1 (the first bubble) and B_2 (the second bubble) during the jet formation processes. Reasonably good agreement was observed during the expansion and early stage of collapse of B_1 with jet formation. In comparison, the initial expansion of B_2 is slightly slower and the later collapse of B_1 toward touchdown is faster in the model simulation than the experimental observations.

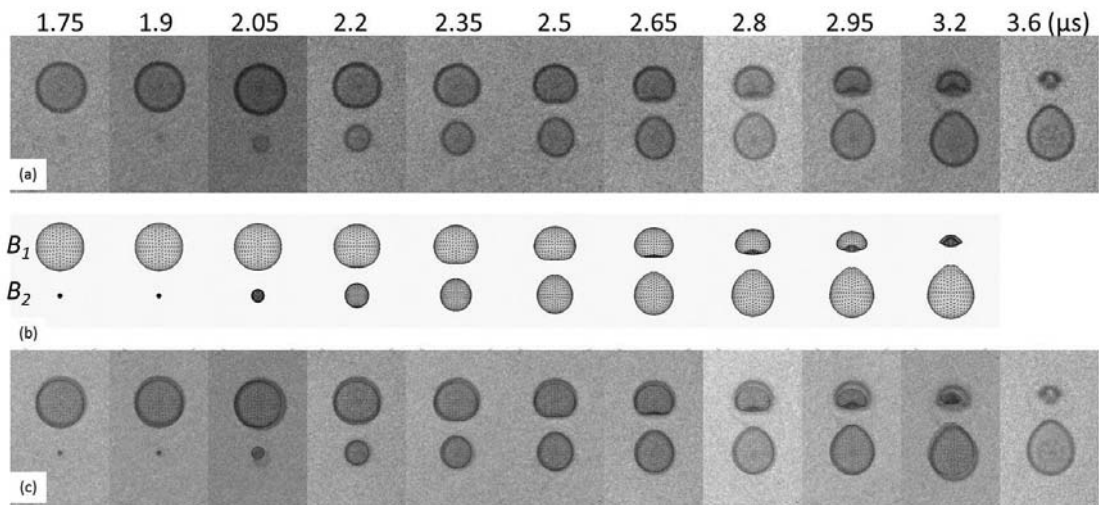


Figure 16 Experiment-Simulation comparison for $D_1 = 40 \mu\text{m}$, $D_2 = 40 \mu\text{m}$ bubble interaction. (a) Experimental results; (b) Simulation results; (c) Superposition of experimental and simulation results.

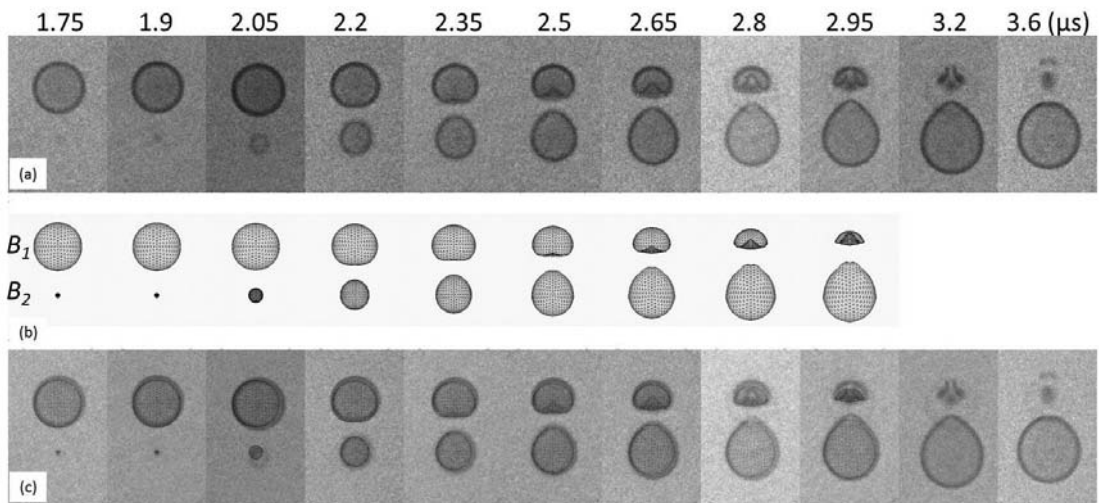


Figure 17 Experiment-Simulation comparison for $D_1 = 40 \mu\text{m}$, $D_2 = 52 \mu\text{m}$ bubble interaction. (a) Experimental results; (b) Simulation results; (c) Superposition of experimental and simulation results.

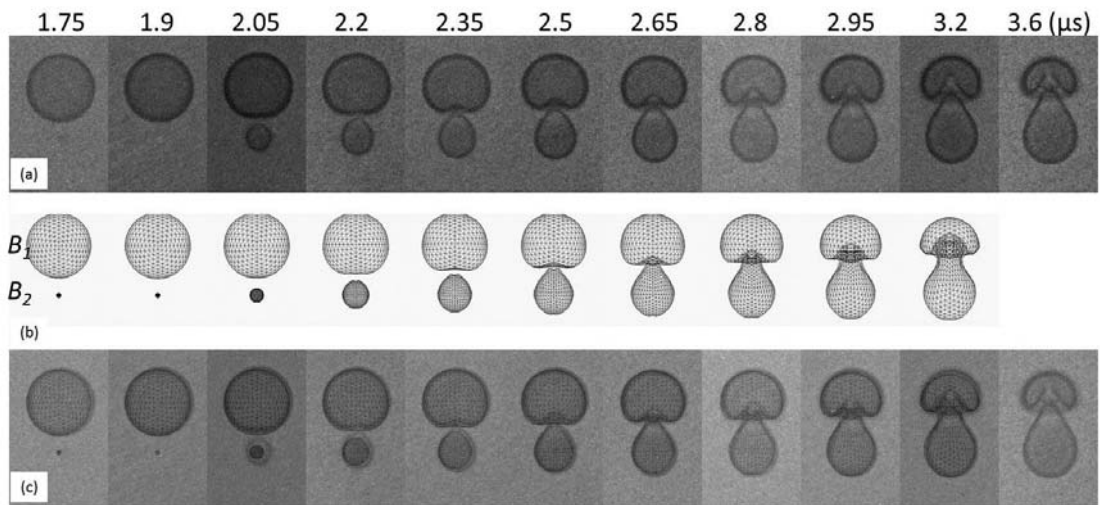


Figure 18 Experiment-Simulation comparison for $D_1 = 56 \mu\text{m}$, $D_2 = 44 \mu\text{m}$ bubble interaction. (a) Experimental results; (b) Simulation results; (c) Superposition of experimental and simulation results.

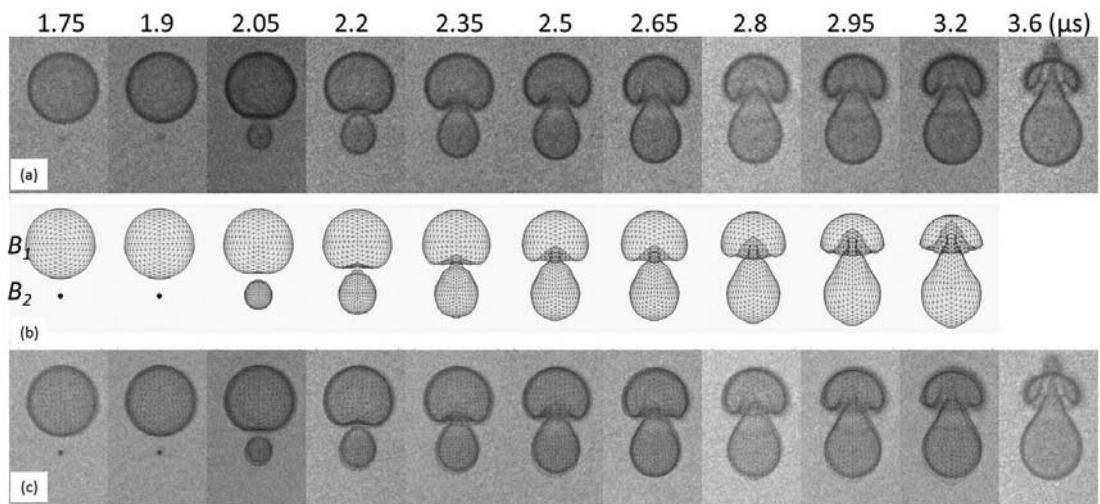


Figure 19 Experiment-Simulation comparison for $D_1 = 56 \mu\text{m}$, $D_2 = 56 \mu\text{m}$ bubble interaction. (a) Experimental results; (b) Simulation results; (c) Superposition of experimental and simulation results.

Based on these observations, we felt that the 3DynaFS-BEM model could be used reasonably to simulate the tandem bubble interaction.

4.2.2 Jet Speed Comparison

The average speed of the jet tip advancing from initiation to touchdown was determined from both experimental data and model simulation results. As shown in Figure 20, the center axis of the tandem bubble is defined by a line connecting the original centers (i.e., gold dots) of the two bubbles. This center axis intersects with the first bubble (bubble 1 or B_1) surface at two points: the proximal end, which is closer to the second bubble (bubble 2 or B_2), and the distal end further away from B_2 . From the results of each experiment, the positions of the proximal and distal ends of B_1 with respect to the original center of B_2 were measured frame by frame. A linear fit of the proximal and distal end positions was made, as shown in Figure 21, from which the touchdown time of J_1 could be determined. The average speed of J_1 was determined by the slope of the fitted line for the proximal end positions. In this study, “jet speed” is used to describe the average speed at the jet tip unless otherwise specified.

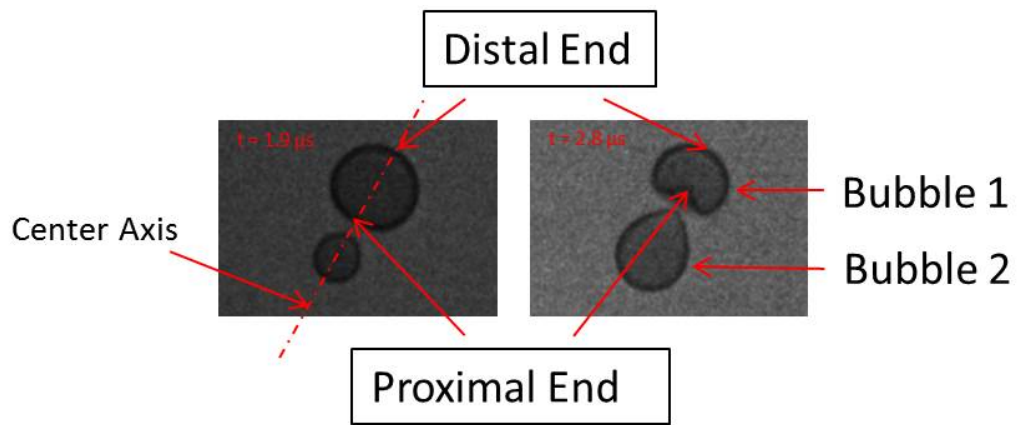


Figure 20 Images of tandem bubbles illustrating the center axis, and proximal end and distal ends of bubble 1.

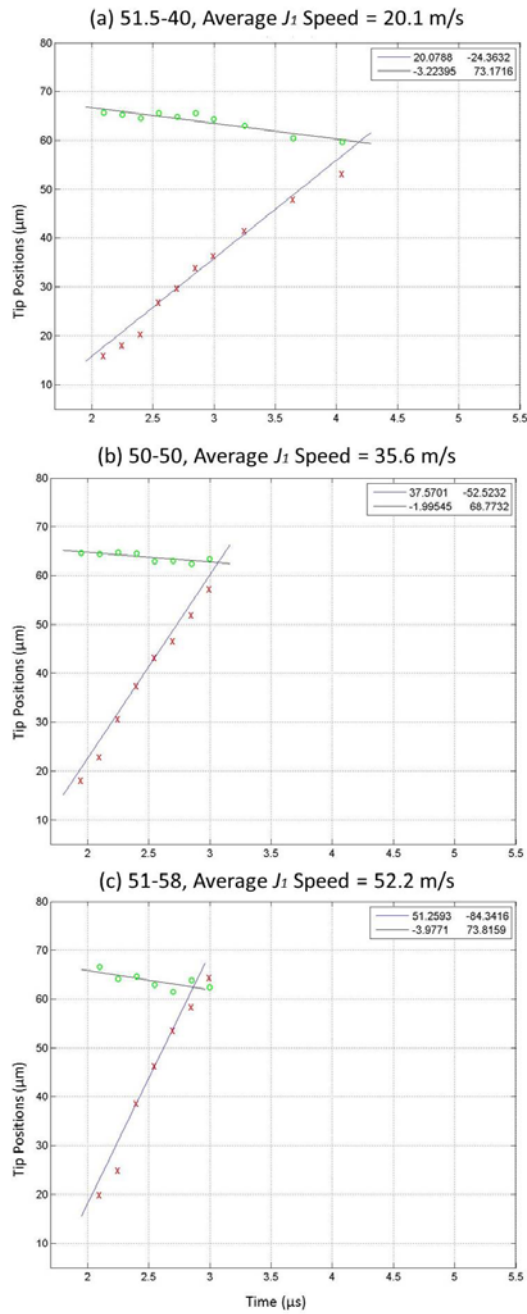


Figure 21 Variation of bubble 1 tip positions for the proximal (in red) and distal (in green) ends with time and the linear fits for determining the touchdown time and the average speed of J_1 .

Based on all the experimental data obtained from tandem bubbles in the size range of 40 to 60 μm , the relationship between the average speed of J_1 and the maximum bubble diameters was determined and plotted in Figure 22.

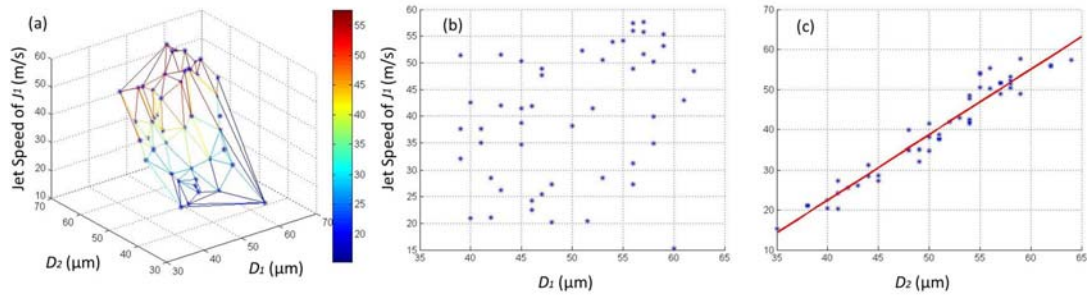


Figure 22 Experimentally measured jet speed vs. D_1 and D_2 . (a) Jet speed vs. D_1 and D_2 ; (b) Jet speed vs. D_1 ; (c) Jet speed vs. D_2 .

The jet speed was found to have a linear correlation with D_2 but no clearly identifiable correlation with D_1 . The jet speed was found to increase from 20 to 58 m/s when D_2 was increased from 40 to 60 μm .

In the model simulation, the speed of the jet tip could be calculated using two different approaches, one based on the speed determined from the time-varying positions of the tip node, or the other determined by the equivalent tip position averaged from the 6 adjacent nodes around the tip. Because of the numerical errors and singularity associated with the meshing of the jet tip, the second approach was used to calculate the speed of the jet tip in the model simulation.

From Figure 21, 23 and 24, it was found that jet speed was nearly constant from jet initiation to touchdown in both experimental and model simulation results, so it was reasonable to represent jet speed at each (D_1, D_2) combination with an average speed. The average speed of the jet in the model simulation was calculated using the following equation:

$$V_{jet} = \frac{x_N - x_1}{t_N - t_1} \quad (4.1)$$

where V_{jet} denotes the average jet speed, t_1 and t_N are the time when the jet starts to form and touchdown, x_1 and x_N are the jet tip positions at t_1 and t_N , respectively.

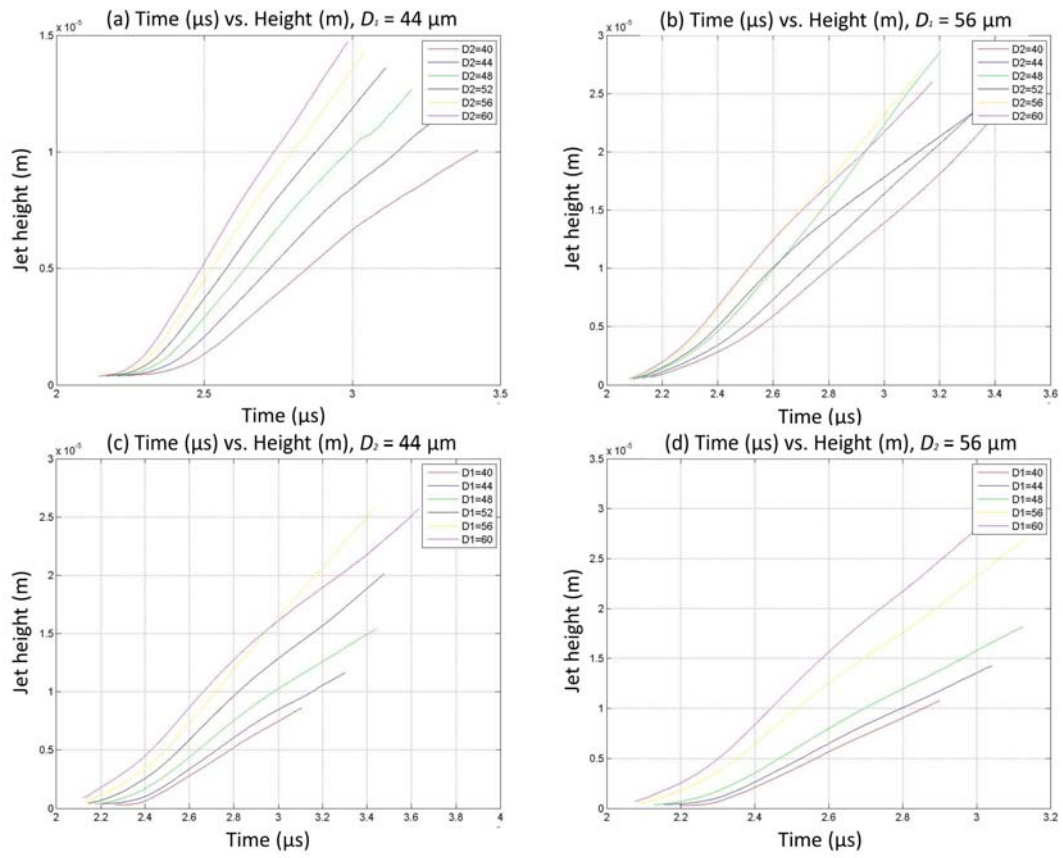


Figure 23 Examples of jet tip position vs. time, collected with one of the bubble sizes fixed. (a) $D_1 = 44 \mu\text{m}$; (b) $D_1 = 56 \mu\text{m}$; (c) $D_2 = 44 \mu\text{m}$; (d) $D_2 = 56 \mu\text{m}$.

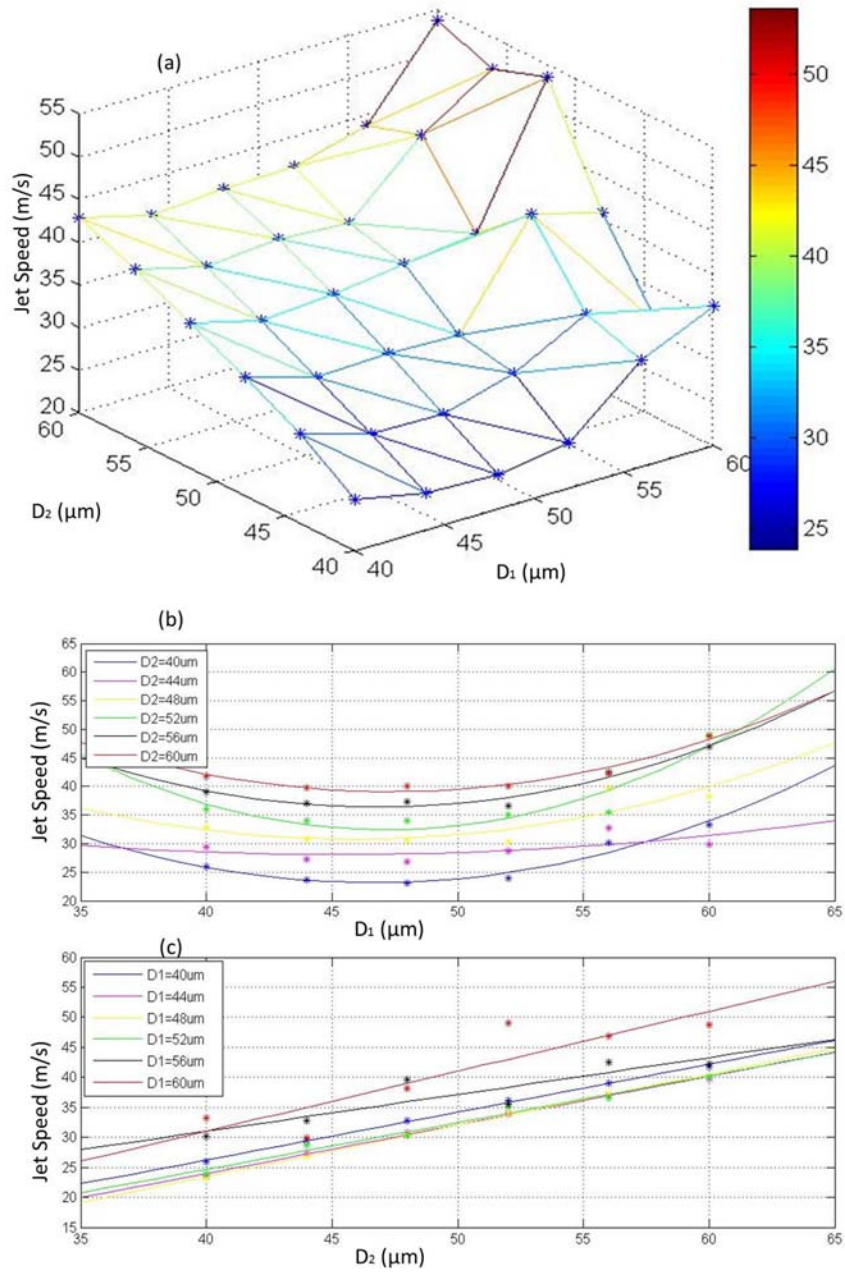


Figure 24 Correlation between jet speed and maximum bubble sizes (D_1 and D_2). (a) Contour plot of jet speed vs. D_1 and D_2 ; (b) Jet speed vs. D_1 at different D_2 values; (c) Jet speed vs. D_2 at different D_1 values.

From Figure 24, it can be seen that the speed increased from 25 to 50 m/s when D_2 is increased from 40 to 60 μm . The jet speed varies linearly with D_2 . The jet speed varied slightly with D_1 except the when D_1 was as large as around 60 μm an abrupt rise was brought to the speed.

From the comparison of Figure 22 and 24, it can be seen that the speed is determined predominately by D_2 and much less influenced by D_1 in both experimental and model simulation results. From Figure 22(a), when different values of D_1 are studied, it can be seen that the smaller D_1 gave better linearity to the correlation of jet speed vs. D_2 . As shown in Figure 22(a) and Figure 24 (a), the values of jet speeds matched with each other well except that simulated jet speed is smaller than experimental jet speed when $D_2 < 50 \mu\text{m}$. This discrepancy may be caused by the neglect of viscosity in 3DynaFS-BEM: when bubble sizes were small, the viscosity loss was large relative to the overall energy of the bubbles, so it would bring a more obvious retarding effect on jet speed, while when bubble sizes were large, such effects would be less evident.

4.2.3 Analysis of Simulated Jet Parameters

From the experiments, the tandem bubble interaction could only be observed from the top view at a limited time steps (confined by 14 total frames of images in each sequence). In comparison, more detailed analysis of the tandem bubble interaction could be obtained from numerical simulations with much finer time steps (corresponding to a

total 120 to 300 frames in each sequence). In addition, the simulation results can be rendered in 3D displays and viewed from different perspectives. Taking advantage of these unique features in model simulation, a detailed analysis of the time evolution in jet geometry was carried out and the momentum and kinetic energy associated with the advancing jet were calculated in relation to different bubble sizes.

To describe jet geometry, several new parameters are defined from the top view (Fig. 25) and side view (Fig. 26), respectively.

First, a base plane perpendicular to the center axis of the tandem bubble can be introduced during the asymmetric collapse of B_1 , which intersects with the proximal side of the bubble at the base line formed by a series of inflection points, as shown in Figure 25. The jet base is defined as being flat and is obtained by the area enclosed by the inflection points, which are defined to be the tangent points of the base line on the bubble where the jet is formed.

Second, the jet height (h) is defined as the shortest distance along the jet direction from jet tip to the base plane.

Third, because jet formed in the microfluidic channel by the tandem bubble interaction is not axisymmetric, two sets of parameters are introduced to describe the shape of the jet from both the top- and side- view, respectively as shown in Figure 26. These parameters are:

- Base radius from top view ($BR-tv$): half of the base width or distance from a jet inflection point to the center axis of the tandem bubble.
- Halfway radius from top view ($HR-tv$): half of the jet width at half of the jet height (h) from jet tip.
- Radius ratio from top view ($RR-tv$): $= HR-tv/BR-tv$ ($0 < RR-tv \leq 1$). $RR-tv$ indicates the shape of the jet from top view. The closer $RR-tv$ is to 1, the more cylindrical the jet shape is seen from top view. In contrast, the closer $RR-tv$ is to 0.5, the more triangular the jet shape is seen from top view.
- Base Radius from Side View ($BR-sv$), halfway radius from side view ($HR-sv$) and radius ratio from side view ($RR-sv$) are defined similarly as shown in Figure 26. As described in Chapter 2, the maximum projected diameters in the top view of the two bubbles generated individually in the microfluidic channel are denoted by D_1 and D_2 .

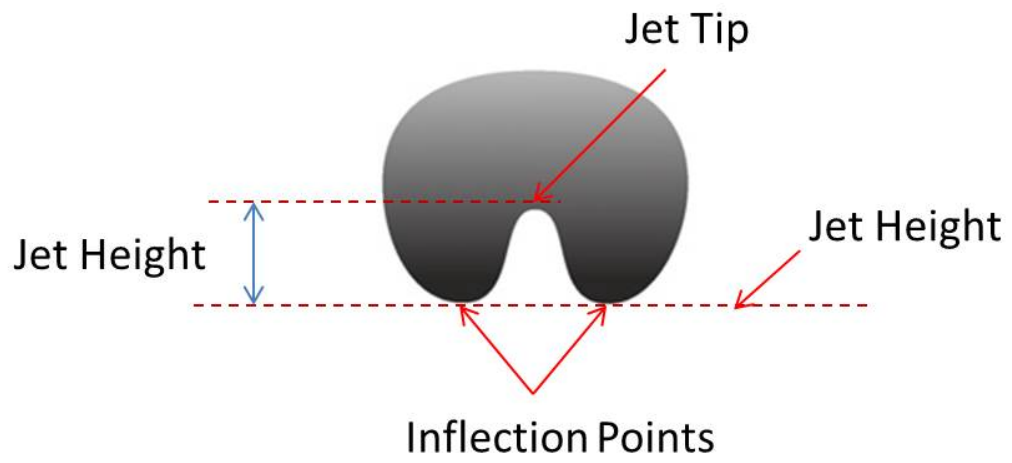


Figure 25 Definition of different parameters that are used to describe jet geometry in 3DynaFS-BEM

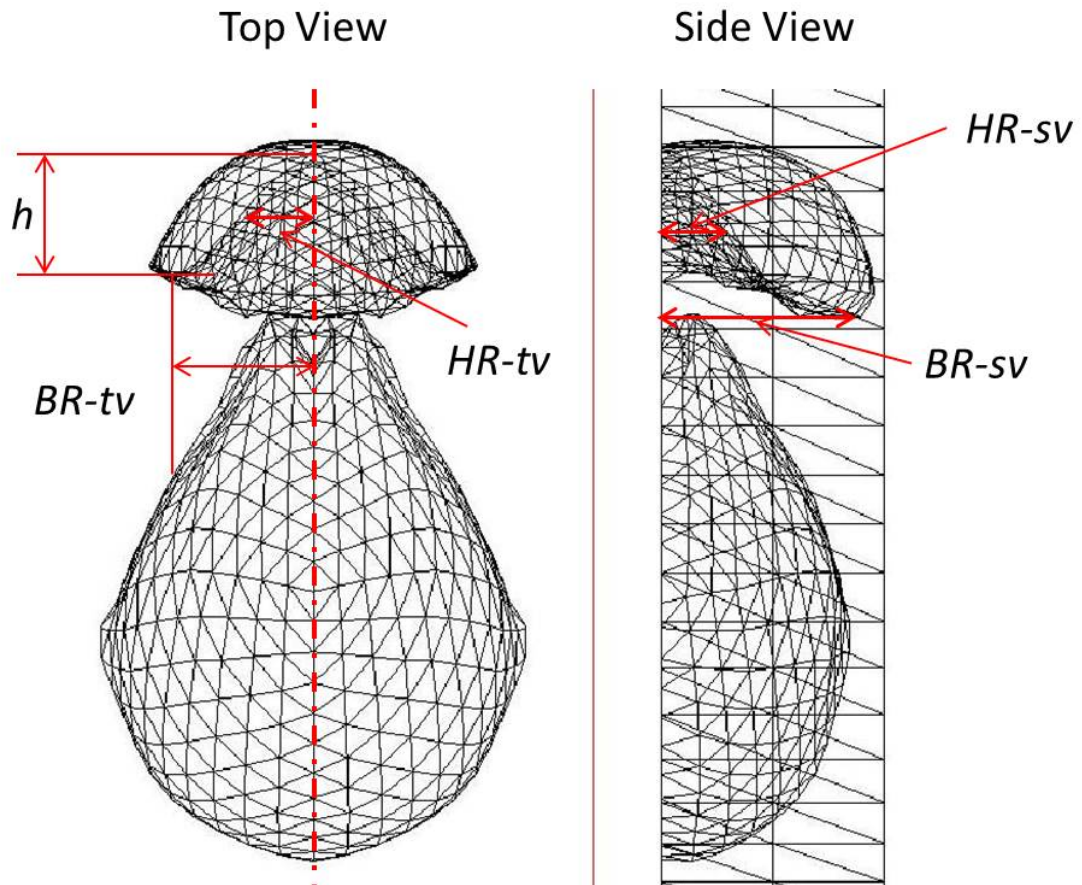


Figure 26 Definition of jet geometry parameters

Figure 27 shows a panel of 36 combined top and side views of the jet geometry at touchdown for different combinations of D_1 and D_2 in the range of 40 to 60 μm with an increment step of 4 μm . The bubble sizes are listed at the top left corner in each frame in the form of D_1 - D_2 . For instance, "40-60" means $D_1 = 40 \mu\text{m}$ and $D_2 = 60 \mu\text{m}$. The effect of D_1 on the jet formation is shown horizontally in each row for a given D_2 . Alternatively, the effect of D_2 can be seen vertically in each column for a given D_1 . The most interesting

observation is the transition of jet geometry from conical to cylindrical shape when D_1 increases, except for the case of 60-60. For instance, in the first row, 40-40, 44-40, and 48-40 are conical jets, 60-40 is a cylindrical jet, 52-40 and 56-40 are transition from conical to cylindrical shapes, and this is true for all the values of D_2 . Moreover, jet height (h) is also found to increase with D_1 .

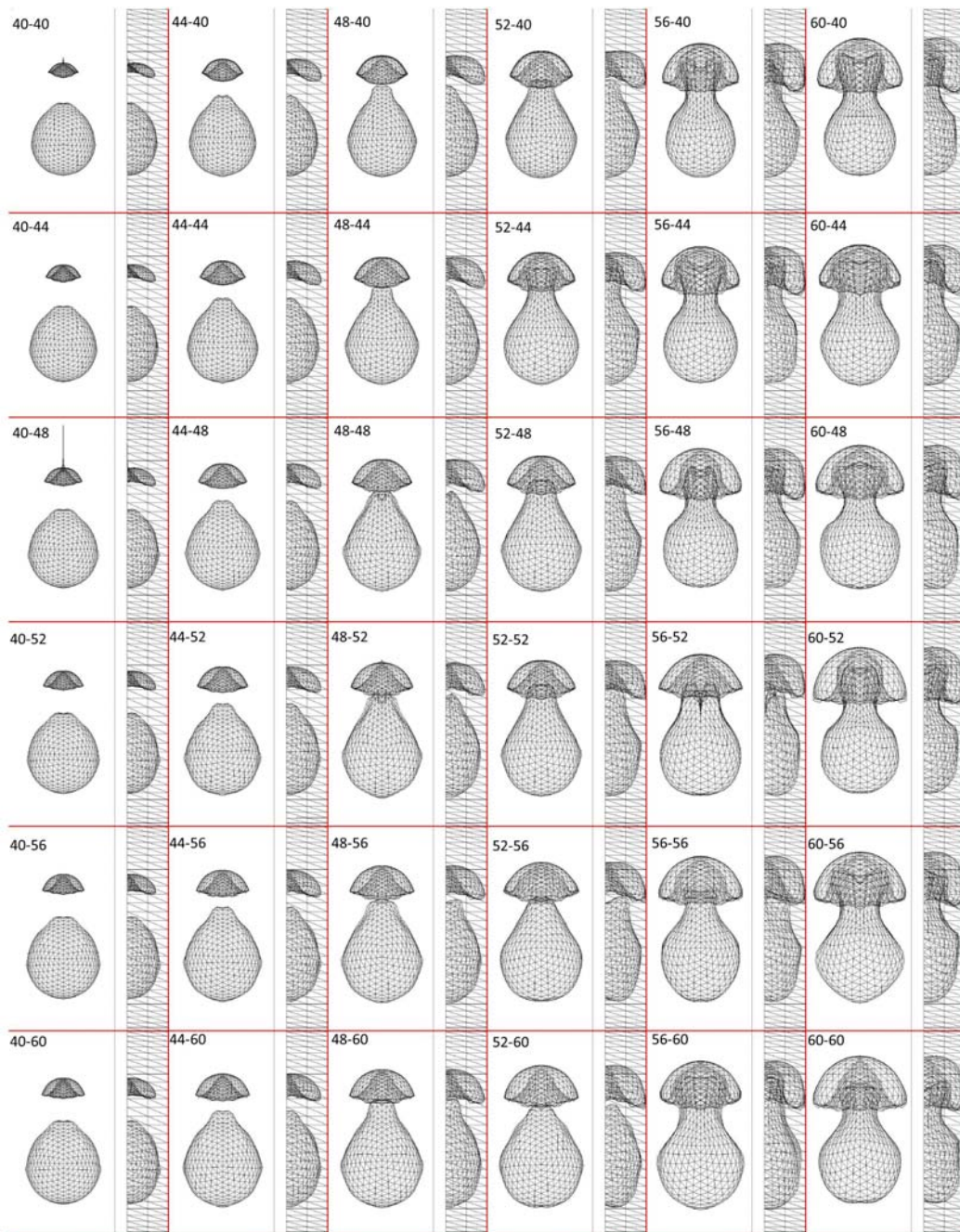


Figure 27 Jet Shape comparison at touchdown: left corner shows the maximum bubble sizes in the form of D_1 - D_2 .

a) Jet Volume (V) vs. Jet Height (h)

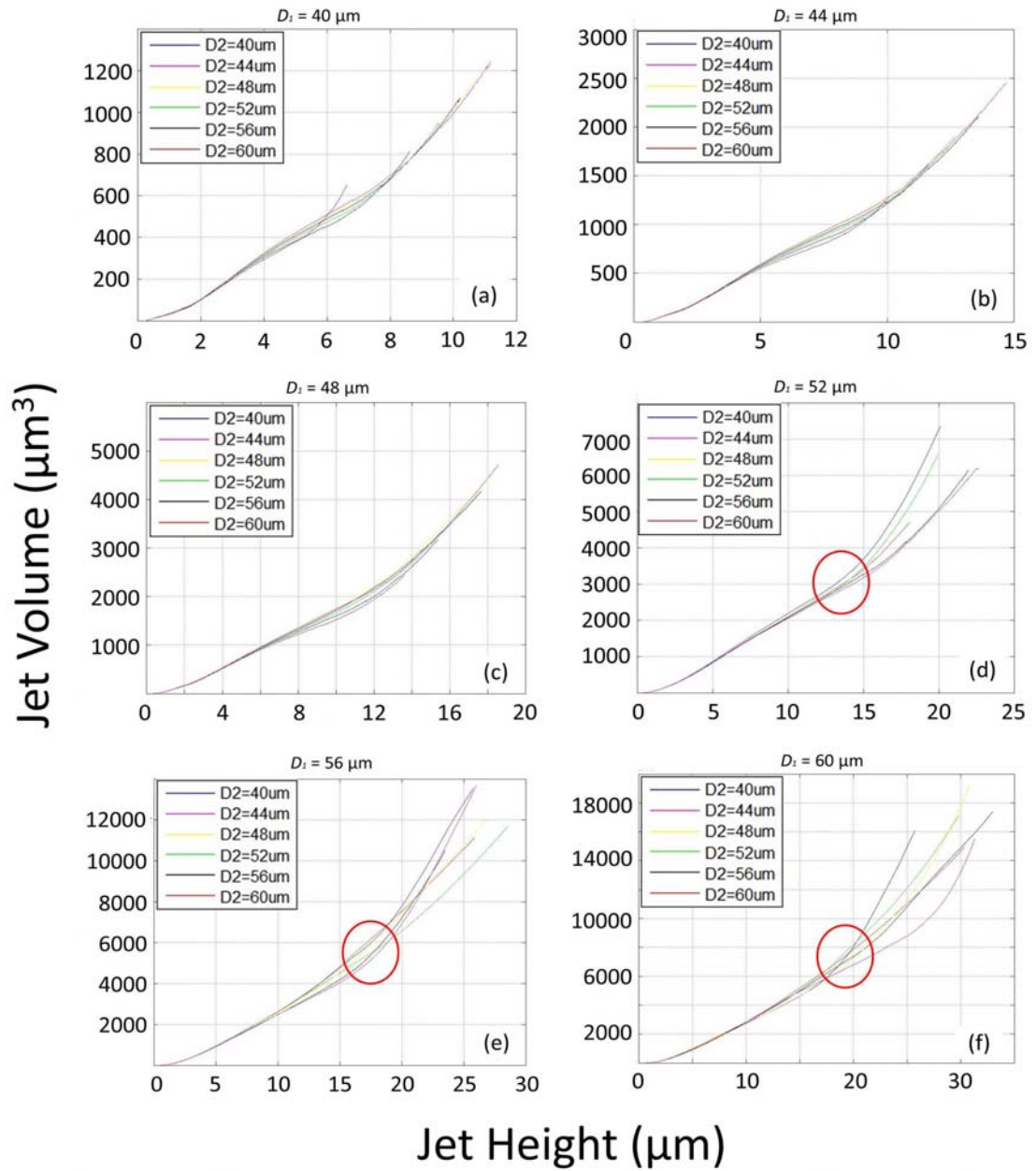


Figure 28 Correlation between jet volume (V) and jet height (h) at different values of D_i .

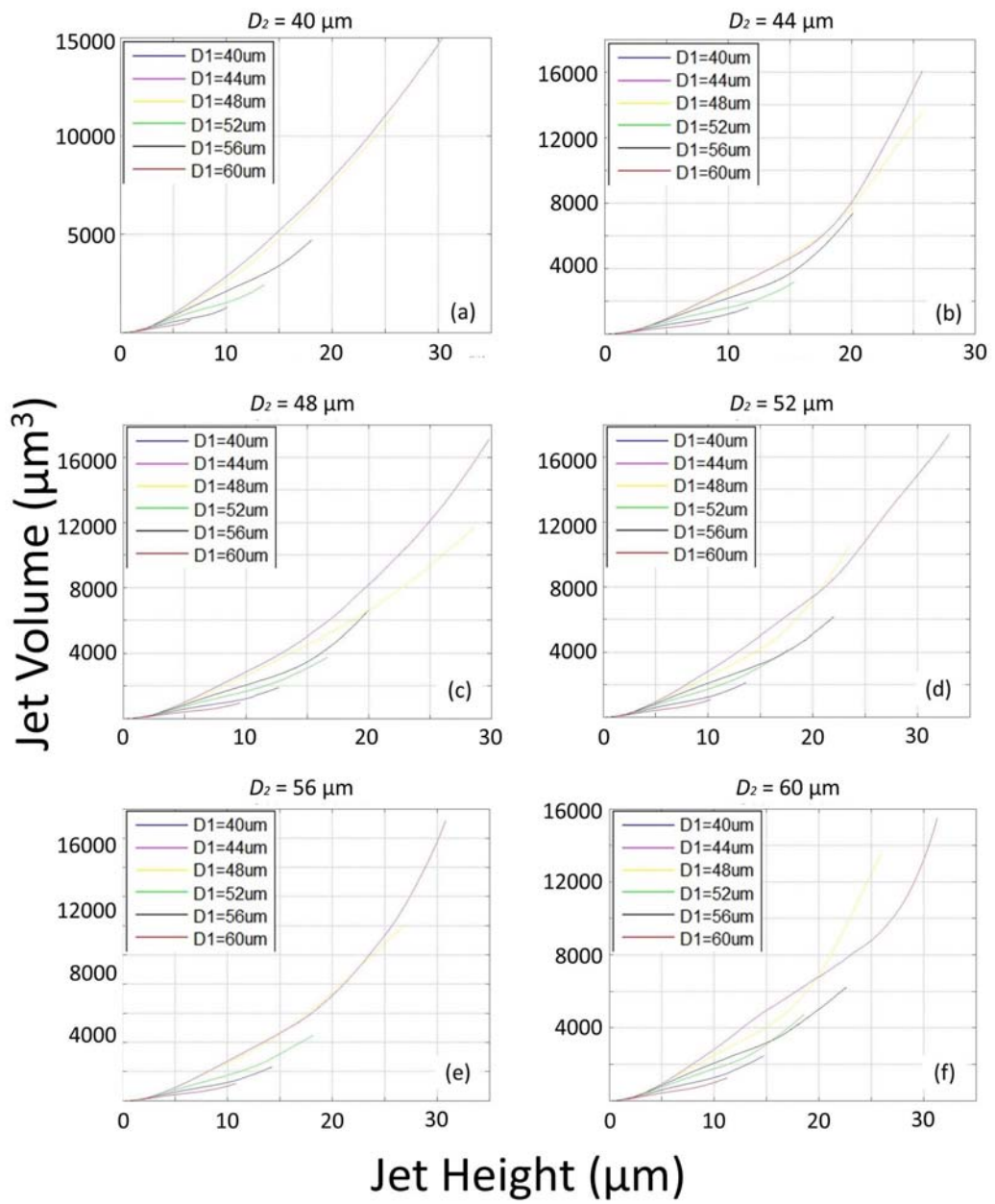


Figure 29 Correlation between jet volume (V) and jet height (h) at different values of D_2

From the model output, we have further calculated the volume of the jet between the tip and base of the jet. The results are plotted in relation to jet height with a set of either fixed D_1 (Fig. 28) or D_2 (Fig. 29) values. In Figure 28 (a)-(c) where D_1 is less than 50 μm , all the curves with different D_2 values were found to follow the same trajectory, suggesting that the corresponding jets might have a similar shape. In Figure 28 (d)-(f) where D_1 is greater than 50 μm , all the curves with different D_2 values were also found to follow the same trajectory until a diverging point indicated by a red circle, at which the shapes of corresponding jets might begin to change. These specifications are supported by the images of jet geometry at touchdown for different sets of D_1 and D_2 values (see Fig. 27). As shown in Figure 13 and Figure 27, B_1 was in a hemispherical shape before its apex touched the channel wall. In another word, $D_1 = 50 \mu\text{m}$, when B_1 's maximum radius was equal to channel height $H = 25 \mu\text{m}$, was the transition point of B_1 's shape. This explained that jet shapes began to diverge around the point of $D_1 = 50 \mu\text{m}$. In addition, as D_1 increases the diverging point moves up to larger h value, indicating the point of jet shape divergence is delayed at larger D_1 .

In contrast, when D_2 was fixed, the curves with different D_1 were clearly separated from each other starting from the very beginning of jet formation. This feature is consistently observed in all cases, suggesting that D_1 is more dominant than D_2 in determining the shape of the jet.

b) Parameters Associated with Jet Geometry

In this section, several specific parameters of the jet are plotted against D_1 and D_2 in a contour plot, followed by their dependency on D_1 and D_2 , respectively.

Top View Parameters:

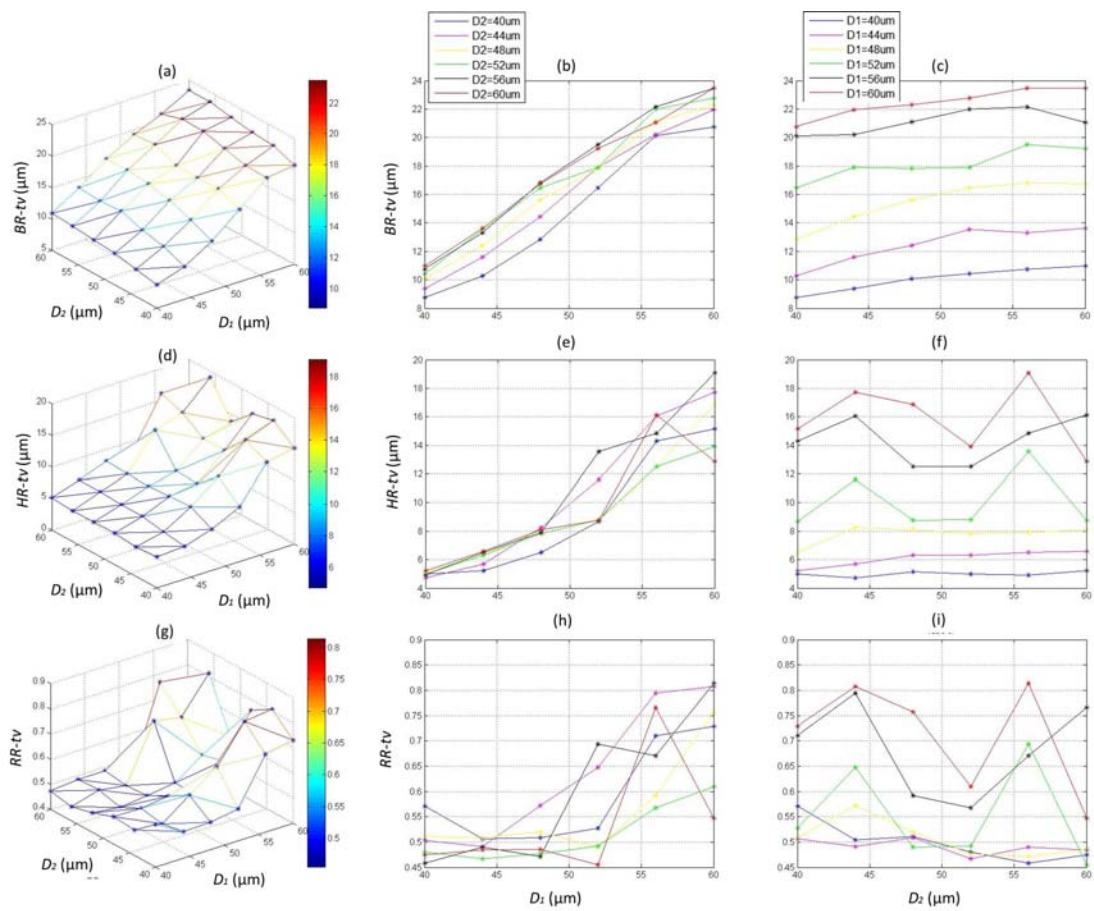


Figure 30 Correlation between top view jet parameters' and maximum bubble sizes (D_1 and D_2). (a), (d) and (g) are the 3-D plots of $BR-tv$, $HR-tv$ and $RR-tv$'s correlations with D_1 and D_2 ; (b), (e) and (h) are the corresponding images projected along D_2 -axis; (c), (f) and (i) are the corresponding images projected along D_1 -axis.

Side View Parameters:

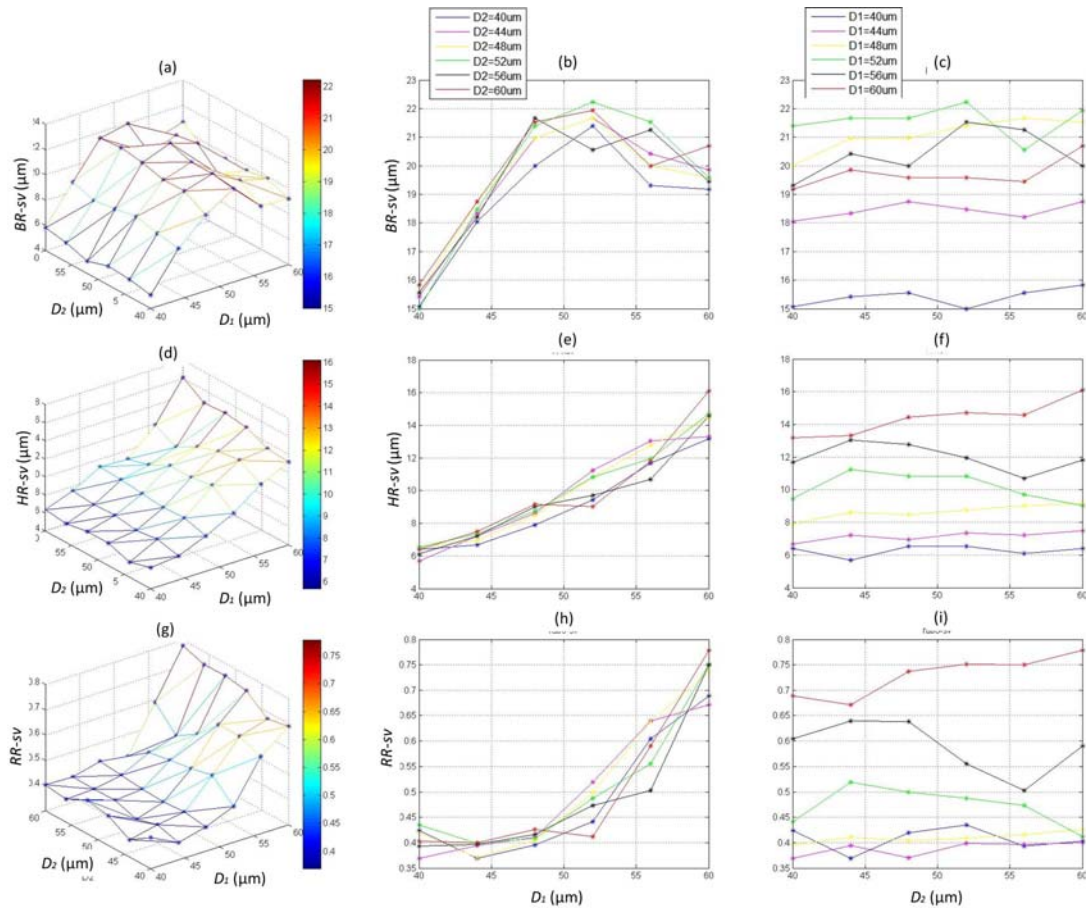


Figure 31 Correlation between side view jet parameters' and maximum bubble sizes (D_1 and D_2). (a), (d) and (g) are the 3-D plots of $BR-sv$, $HR-sv$ and $RR-sv$'s correlations with D_1 and D_2 ; (b), (e) and (h) are the corresponding images projected along D_2 -axis; (c), (f) and (i) are the corresponding images projected along D_1 -axis.

Figures 30 and 31 show, from the top and side views, respectively, the base radius (BR), halfway radius (HR) and radius ratio (RR) of the jets produced by tandem bubble interactions under different sets of D_1 and D_2 . In general, these jet parameters were found to be influenced more significantly by D_1 and much less so by D_2 . It can be noted that the values of $RR-tv$ and $RR-sv$ were close to 0.5 when D_1 was less than 50 μm ,

and increased significantly when D_1 became larger than $50 \mu\text{m}$ (see Fig. 30(h) and 31(h)).

This result is consistent with the observation that the jet shape was more conical if the maximum expansion of B_1 was less than the channel height and more cylindrical after B_1 touched the top surface of the channel (see Fig. 27, horizontal direction from left to right).

c) Maximum Jet Volume, Jet Height and Base Radius

Other than jet speed and jet shape, the amount of fluid moving with the jet is also an important parameter that influences the effect of sonoporation, so the maximum jet volume (Vol_{max}) defined by the volume of fluid enclosed by the jet boundaries at touchdown, and also two associated parameters maximum jet height (h_{max}) and maximum base radius (BR_{max}) will be studied against D_1 and D_2 in this section.

Maximum Jet Volume:

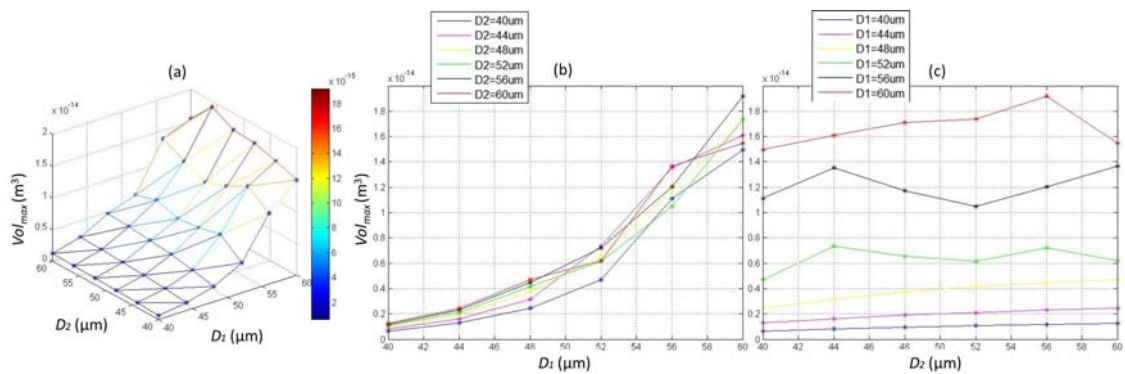


Figure 32 Correlation between maximum jet volume and maximum bubble sizes (D_1 and D_2). (a) Vol_{max} vs. D_1 and D_2 ; (b) Vol_{max} vs. D_1 ; (c) Vol_{max} vs. D_2 .

As shown in Figure 32, Vol_{max} was found to increase almost linearly with D_1 before $D_1 = 50 \mu\text{m}$, and more rapidly with after $D_1 = 50 \mu\text{m}$; Vol_{max} was almost flat in its correlation curve with D_2 . It can be concluded that Vol_{max} was more sensitive to D_1 and less so to D_2 , and a transition existed at around $D_1 = 50 \mu\text{m}$.

Maximum Jet Height:

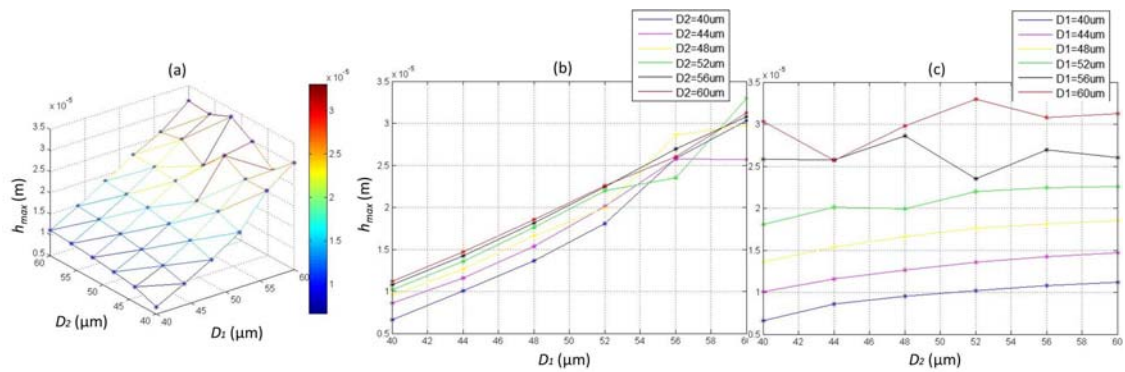


Figure 33 Correlation between maximum jet height and maximum bubble sizes (D_1 and D_2). (a) h_{max} vs. D_1 and D_2 ; (b) h_{max} vs. D_1 ; (c) h_{max} vs. D_2 .

Maximum Base Radius (from top view):

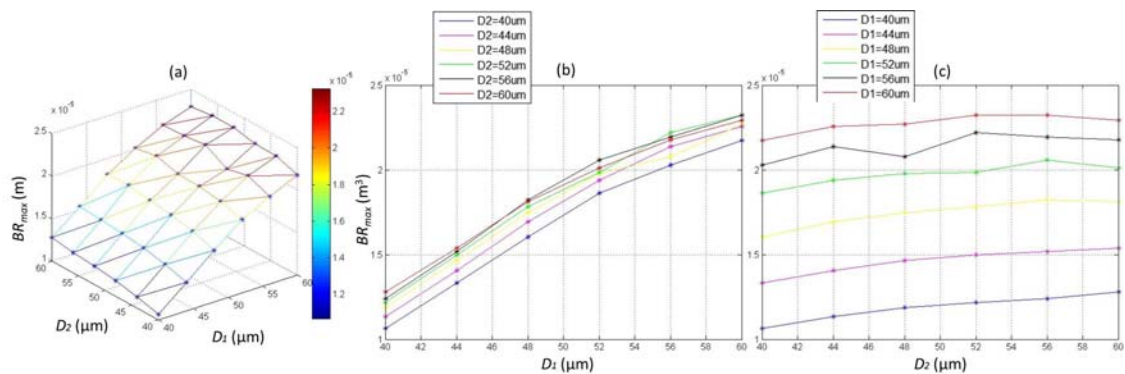


Figure 34 Correlation between maximum jet base radius and maximum bubble sizes (D_1 and D_2). (a) BR_{max} vs. D_1 and D_2 ; (b) BR_{max} vs. D_1 ; (c) BR_{max} vs. D_2 .

As shown in Figure 33 and 34, h_{max} and BR_{max} were found to increase almost linearly with D_1 in the range of 40 to 60 μm ; h_{max} and BR_{max} were almost flat in their correlation curve with D_2 . It can be concluded that h_{max} and BR_{max} were more sensitive to D_1 and less so to D_2 .

All in all, the results from this section suggest that the jet shape and volume are dominated by D_1 and significantly less influenced by D_2 . When D_1 is less than $2H$, a conical jet is usually formed whereas when D_1 is greater than $2H$ the resultant jet will begin to transform from conical to cylindrical toward the touchdown.

d) Maximum Jet Momentum and Kinetic Energy:

From the point of view of force and energy, the momentum and kinetic energy carried by the jet could also influence sonoporation. In this section, the correlation between the maximum momentum (M_{max}) carried by Vol_{max} and bubble sizes (D_1 and D_2), and the correlation between the maximum kinetic energy (KE_{max}) carried by Vol_{max} and bubble sizes (D_1 and D_2), as shown in Figure 35 and 36 below.

Maximum jet momentum:

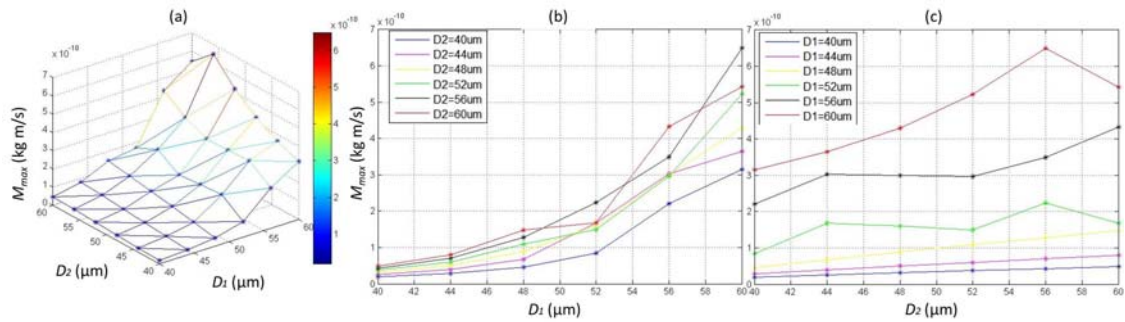


Figure 35 Correlation between maximum jet momentum (M_{max}) and maximum bubble sizes (D_1 and D_2). (a) M_{max} vs. D_1 and D_2 ; (b) M_{max} vs. D_1 ; (c) M_{max} vs. D_2 .

Maximum Kinetic Energy:

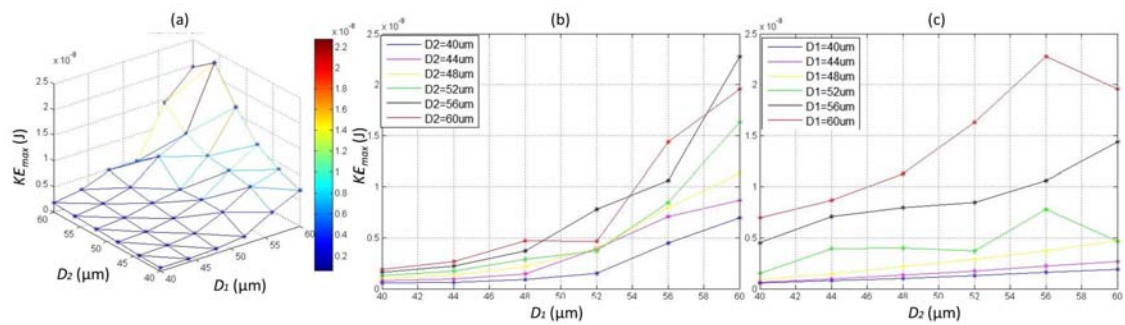


Figure 36 Correlation between maximum jet kinetic energy (KE_{max}) and maximum bubble sizes (D_1 and D_2). (a) KE_{max} vs. D_1 and D_2 ; (b) KE_{max} vs. D_1 ; (c) KE_{max} vs. D_2 .

As shown in Figure 35 and 36, M_{max} and KE_{max} were found to increase with D_1 in the range of 40 to 60 μm , and the increment slopes were larger when D_1 increased after the transition point of $D_1 = 50 \mu\text{m}$; M_{max} and KE_{max} were also found to increase with D_2 in the range of 40 to 60 μm , but almost linearly and not so significantly. The observation that M_{max} and KE_{max} being influenced by both D_1 and D_2 indicates that they are the cumulative effects of velocity and jet volume, which were found to be mainly determined by D_2 and D_1 , respectively.

As Vol_{max} , M_{max} and KE_{max} indicate the volume, momentum and kinetic energy carried by the jet at touchdown, it is also interesting to evaluate the equivalent velocity calculated from the momentum and kinetic energy, as follows:

$$V_{Mom} = \frac{M_{max}}{\rho \cdot Vol_{max}} \quad (4.2)$$

$$V_{KE} = \sqrt{\frac{2KE_{max}}{\rho \cdot Vol_{max}}} \quad (4.3)$$

The correlation between V_{Mom} and V_{KE} and bubble sizes are shown in Figure 37 and 38, respectively.

Equivalent Jet Speed Calculated from Jet Momentum:

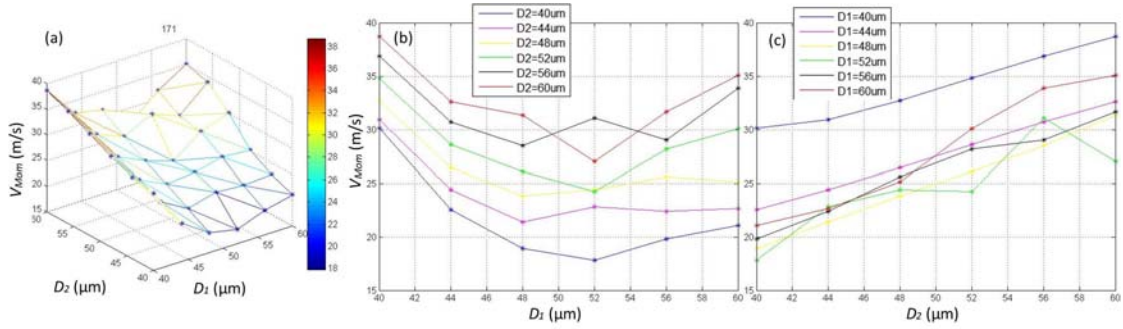


Figure 37 Correlation between equivalent jet speed from momentum (V_{Mom}) and maximum bubble sizes (D_1 and D_2). (a) V_{Mom} vs. D_1 and D_2 ; (b) V_{Mom} vs. D_1 ; (c) V_{Mom} vs. D_2 .

Equivalent Jet Speed Calculated from Jet Kinetic Energy:

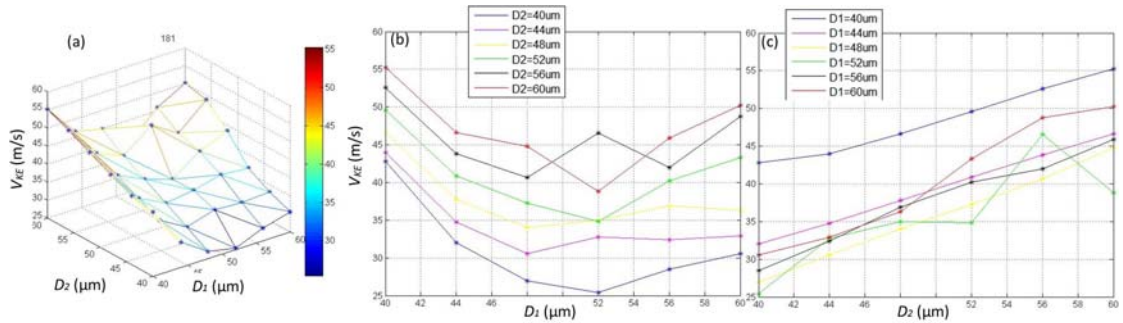


Figure 38 Correlation between equivalent jet speed from kinetic energy (V_{KE}) and maximum bubble sizes (D_1 and D_2). (a) V_{KE} vs. D_1 and D_2 ; (b) V_{KE} vs. D_1 ; (c) V_{KE} vs. D_2 .

As shown in Figure 37 and 38, the trend in the dependence of V_{Mom} and V_{KE} on bubble sizes is very similar, but the values are different. V_{Mom} was found to vary from 18 to 38 m/s, while V_{KE} varied from 25 to 55 m/s with different D_1 and D_2 values. They both increased almost linearly with D_2 for a fixed D_1 . An interesting minimum point was found in both V_{Mom} and V_{KE} 's correlations with D_1 at around $D_1 = 52 \mu\text{m}$. This minimum was also found in the jet tip velocity (see Fig. 24).

5. Conclusion and Future Work

We have investigated both experimentally and numerically the interaction of tandem bubbles in a microfluidic channel made of PDMS and a glass bottom with 25 mm in length, and 25 × 800 μm in height and width, respectively. Gold dots of 15 nm in thickness and 6 μm in diameter were coated on the glass surface with a separation distance of 40 μm. Irradiation of a 5 ns pulsed Nd: YAG laser of 532 nm in wavelength on a gold dot leads to the generation and growth of a single bubble that can reach a maximum diameter in the microfluidic channel in the range of 40 to 60 μm with a corresponding bubble expansion time of 1.8 to 2.2 μs. Irradiation of two adjacent gold dots by two pulsed Nd: YAG lasers with an inter-pulse delay of 2 μs produces tandem bubbles in approximately anti-phase oscillation. The dynamics of tandem bubble interaction and resultant jet formation in the first bubble were captured by high-speed imaging and further analyzed by a numerical model based on boundary element method. The main observations and conclusions of this study are summarized below.

Based on experimental observations, the average speed of the jet tip was found to correlated almost linearly with D_2 (the maximum diameter of the second bubble) but not clearly with D_1 (the maximum diameter of the first bubble). The model simulations have confirmed this observation and further suggest that there is a weak dependency of jet

speed on D_1 with high values obtained at both small and large D_1 (i.e., 40 and 60 μm) and low value obtained at the intermediate size of $D_1 = 50 \mu\text{m}$.

A parametric study of the tandem bubble interaction based on the numerical model suggests that the shape of the jet is determined predominately by D_1 yet minimally influenced by D_2 . In particular, there is a transition of the jet from conical to cylindrical shape when the expansion of the first bubble touches the ceiling of the PDMS channel (i.e., when D_1 reaches 50 μm). The maximum jet height and volume at touchdown were found to correlate approximately linearly with both D_1 and D_2 . However, the dependency of these parameters on D_1 is much stronger than D_2 .

In addition, the trajectory for jet volume-height correlation shows a strong dependency on D_1 (independent on D_2) up to the transition point where $D_1 = 2H = 50 \mu\text{m}$. Beyond the transition point, the trajectories for jet volume-height corresponding to different values of D_2 diverge from each other, reflecting the significant changes in jet geometry.

Furthermore, before the transition point the maximum jet momentum and kinetic energy at touchdown show a strong correlation with D_1 but are minimally influenced by D_2 . Above the transition point the jet momentum and kinetic energy increase more rapidly with both D_1 and D_2 , reflecting the combined contribution of significantly increased jet size and velocity to these two parameters.

Altogether, our results suggest that bubble 1 provides the initial reference frame for tandem bubble interaction with the channel wall and jet formation, and thus it is the critical parameter that determines the shape and volume of the resultant jet. In contrast, bubble 2 provides the driving force for the asymmetric collapse of bubble 1 and is the critical parameter that determines the jet velocity. Both D_1 and D_2 are important in determining the momentum and kinetic energy of the jet, suggesting that treatment of single cells by tandem bubbles should be carried out with well-defined bubble sizes. Alternatively, variations of bubble size may be used to increase the dynamics range of jet-induced stresses that can be applied to single cells placed nearby at a fixed stand-off distance.

For further work, a scale analysis should be performed to help dissecting more clearly the correlation between jet parameters and different bubble sizes during the tandem bubble interaction. Moreover, the flow field produced by tandem bubbles needs to be characterized in order to better understand the stresses imposed on individual cells grown nearby. This knowledge may help to improve the design of tandem bubble treatment on single cells in the future.

Bibliography

- Brennen, Christopher E. *Cavitation and Bubble Dynamics*. New York: Oxford University Press, 1995.
- Hsiao, C-T, et al. "Modeling Single and Tandem Bubble Dynamics between Two Parallel Plates for Biomedical Applications." *Journal of Fluid Mechanics*, 2013: 137-170.
- Miller, D. L. "A review of ultrasonic bioeffects of microsonation, gas-body activation, and." *Ultrasound in medicine & biology*, 1987: 443-470.
- Quinto-Su, Pedro A., Kang Y. Lim, and Ohl Claus-Dieter . "Cavitation bubble dynamics in microfluidic gaps of variable height." *Physical Review*, 2009.
- Sankin, G. N., F. Yuan, and P. Zhong. "Pulsating Tandem Microbubble for Localized and Directional Single-Cell Membrane Poration." *Physical Review Letter*, 2010: 105(7).
- Yang, G.W. "Laser ablation in liquids: Applications in the synthesis of nanocrystals." *Progress in Materials Science*, 2007: 648-698.
- Yuan, Fang. *Probing the Bioeffects of Cavitation at the Single-Cell Level*. Durham: Duke University, 2013.
- Yuan, Fang, Georgy Sankin, and Pei Zhong. "Dynamics of tandem bubble interaction in a microfluidic channel." *The Joournal of the Acoustical Society of America*, 2011: 130.